Draft version January 27, 2026
Typeset using LaTeX **twocolumn** style in AASTeX7.0.1

JWST Spectroscopic Census of ALMA Faint Submillimeter Galaxies in the Hubble Ultra Deep Field

Tomokazu Kiyota [1,2] Masami Ouchi [2,3,1,4] Daisuke Iono [2,1] Seiji Fujimoto [5,6] Kotaro Kohno [7,8] Yoshihiro Ueda [9] Kimihiko Nakajima [10,2] Moka Nishigaki [1,2] and Hidenobu Yajima [11]

[1] *Department of Astronomical Science, The Graduate University for Advanced Studies, SOKENDAI, 2-21-1 Osawa, Mitaka, Tokyo, 181-8588, Japan*
[2] *National Astronomical Observatory of Japan, 2-21-1 Osawa, Mitaka, Tokyo, 181-8588, Japan*
[3] *Institute for Cosmic Ray Research, The University of Tokyo, 5-1-5 Kashiwanoha, Kashiwa, Chiba 277-8582, Japan*
[4] *Kavli Institute for the Physics and Mathematics of the Universe (WPI), University of Tokyo, Kashiwa, Chiba 277-8583, Japan*
[5] *David A. Dunlap Department of Astronomy and Astrophysics, University of Toronto, 50 St. George Street, Toronto, Ontario, M5S 3H4, Canada*
[6] *Dunlap Institute for Astronomy and Astrophysics, 50 St. George Street, Toronto, Ontario, M5S 3H4, Canada*
[7] *Institute of Astronomy, Graduate School of Science, The University of Tokyo, 2-21-1 Osawa, Mitaka, Tokyo 181-0015, Japan*
[8] *Research Center for the Early Universe, Graduate School of Science, The University of Tokyo, 7-3-1 Hongo, Bunkyo-ku, Tokyo 113-0033, Japan*
[9] *Department of Astronomy, Kyoto University, Kyoto 606-8502, Japan*
[10] *Institute of Liberal Arts and Science, Kanazawa University, Kakuma-machi, Kanazawa, Ishikawa, 920-1192, Japan*
[11] *Center for Computational Sciences, University of Tsukuba, Ten-nodai, 1-1-1 Tsukuba, Ibaraki 305-8577, Japan*

(Received —; Revised —; Accepted —; Published —)

Submitted to ApJ

ABSTRACT

We present a JWST/NIRSpec rest-frame optical spectroscopic census of ALMA 1-mm continuum sources in the Hubble Ultra Deep Field (UDF) identified by the deep ALMA UDF and ASPECS programs. Our sample is composed of the ALMA flux-limited ($S_{1\,\mathrm{mm}} \gtrsim 0.1\,\mathrm{mJy}$) sources observed with medium-resolution NIRSpec spectroscopy from JADES and SMILES, 16 faint submillimeter galaxies (SMGs) at spectroscopic redshifts of $z \sim 1$–4. These SMGs show bright longer-wavelength optical lines (Hα, [N II]$\lambda\lambda$6548, 6583, and [S II]$\lambda\lambda$6717, 6731) and faint shorter-wavelength optical lines (Hβ and [O III]$\lambda\lambda$4959, 5007) with a large nebular attenuation, $E(B-V) \sim 0.3$–1.8. We test the SMGs using BPT diagnostics and Chandra X-ray fluxes, and find that most SMGs are classified as AGNs; the AGN fraction is $\sim 80\%$ for the SMGs at $M_* > 10^{10.5} M_\odot$. We find only one SMG ($< 10\%$) with a broad Balmer line, indicating that the SMGs are predominantly obscured AGNs. With the optical lines, we estimate the metallicities of the SMGs to be moderately high, ~ 0.4–$2 Z_\odot$, exceeding the model-predicted dust-growth critical metallicity (~ 0.1–$0.2 Z_\odot$), which naturally explains the dusty nature of the SMGs. Interestingly, the SMGs fall in the mass-metallicity relation and the star-formation main sequence, showing no significant differences from other high-z galaxies. Similarly, we find electron densities of $n_e \sim 10^2$–$10^3\,\mathrm{cm}^{-3}$ for the SMGs that are comparable with other high-z galaxies. Together with the high SMG fraction ($\sim 100\%$) at the massive end ($M_* > 10^{10.5} M_\odot$), these results indicate that the SMGs are mostly not special, but typical massive star-forming galaxies at high redshift.

Keywords: Galaxy evolution (594) — Galaxy formation (595) — High-redshift galaxies (734)

1. INTRODUCTION

Over the past few decades, large (sub)millimeter continuum surveys have been carried out with single-dish telescopes and interferometers such as the Submillimetre Common-User Bolometer Array (SCUBA; W. S. Hol-

Email: tomokazu.kiyota@grad.nao.ac.jp

land et al. 1999), the South Pole Telescope (SPT; J. E. Carlstrom et al. 2011), and, more recently, the Atacama Large Millimeter/submillimeter Array (ALMA; A. Wootten & A. R. Thompson 2009). These surveys detect rest-frame far-infrared (FIR) dust emission from high-redshift ($z \gtrsim 1$) galaxies and provide constraints on their dust-obscured star formation and cold interstellar medium (ISM; e.g., A. W. Blain & M. S. Longair 1993; I. Smail et al. 1997; A. W. Blain et al. 2002; S. Fujimoto et al. 2016, 2017; J. S. Dunlop et al. 2017; B. Hatsukade et al. 2018; M. Aravena et al. 2019, 2020; R. Bouwens et al. 2020; U. Dudzevičiūtė et al. 2020; S. Fujimoto et al. 2024, 2025).

The bright dust-continuum sources, commonly referred to as submillimeter galaxies (SMGs), contain large dust and molecular gas reservoirs and sustain extreme star-formation rates of 10^2–10^3 $M_\odot$ yr^{-1} (C. M. Casey et al. 2014; J. A. Hodge & E. da Cunha 2020 for reviews). Their large stellar and gas masses, short gas-depletion timescales, and number densities suggest that high-redshift SMGs are plausible progenitors of the quiescent and massive elliptical galaxies observed at lower redshifts (e.g., P. F. Hopkins et al. 2008; S. Toft et al. 2014; C. Gómez-Guijarro et al. 2018; U. Dudzevičiūtė et al. 2020). In this context, high-redshift dusty galaxies, including SMGs, are key laboratories for understanding the evolutionary pathway of massive galaxies.

ALMA has further revealed this population down to fainter dust-continuum sources, and extensive observations are conducted with multi-wavelength facilities. One remarkable example is the Great Observatories Origins Deep Survey (GOODS; M. Giavalisco et al. 2004) south (GOODS-S) field, especially in the Hubble Ultra Deep Field (HUDF; S. V. W. Beckwith et al. 2006). In this field, deep ALMA dust continuum (e.g., F. Walter et al. 2016; J. S. Dunlop et al. 2017; B. Hatsukade et al. 2018; M. Franco et al. 2018; M. Aravena et al. 2020; J. González-López et al. 2020; C. Gómez-Guijarro et al. 2022a), CO lines (e.g., M. Aravena et al. 2019; L. A. Boogaard et al. 2019; R. Decarli et al. 2019), Chandra X-ray Observatory (Chandra; e.g., M. C. Weisskopf et al. 2002) data (e.g., R. Giacconi et al. 2002; B. D. Lehmer et al. 2005; S. X. Wang et al. 2013; B. Luo et al. 2017; Y. Ueda et al. 2018), and the Hubble Space Telescope (HST) rest-optical to near-infrared (NIR) imaging (e.g., N. A. Grogin et al. 2011; G. D. Illingworth et al. 2013) exist. These data provide multi-wavelength spectral energy distributions (SED) from ultraviolet (UV) to FIR, as well as key FIR emission lines, which reveal stellar populations, molecular gas, and dust content. However, these surveys and bright SMGs observations lack the overall rest-frame optical emission lines (e.g., C. M. Casey et al. 2017).

Rest-frame optical emission lines provide powerful diagnostics of gas-phase metallicity, ionization state (e.g., M. Curti et al. 2020; R. L. Sanders et al. 2021; K. Nakajima et al. 2023; M. Nishigaki et al. 2025), electron density (e.g., M. W. Topping et al. 2025), and the presence of active galactic nuclei (AGN; e.g., V. Kokorev et al. 2023), but such measurements have been challenging for SMGs: strong dust attenuation renders their rest-UV/optical continua and lines faint, and these diagnostics are redshifted into the NIR, where even 8–10 m class ground-based telescopes had limited sensitivity and wavelength coverage. Thus, even basic quantities of dust-continuum sources remain poorly constrained (see also, e.g., A. M. Swinbank et al. 2004; C. M. Casey et al. 2017; A. E. Shapley et al. 2020).

The James Webb Space Telescope (JWST; J. P. Gardner et al. 2023) has dramatically changed this situation. Its NIR sensitivity and spectral coverage enable us to investigate rest-frame optical nebular lines in high-redshift dusty galaxies. Early JWST/Near Infrared Spectrograph (NIRSpec; P. Jakobsen et al. 2022) observations have started to probe the ionized gas conditions and central powering sources for the bright SMGs (e.g., S. Arribas et al. 2024; G. C. Jones et al. 2024; H. Übler et al. 2024; G. C. Jones et al. 2025; E. Parlanti et al. 2024, 2025; O. R. Cooper et al. 2025 and see also JWST imaging studies, e.g., C. Cheng et al. 2023; W. Rujopakarn et al. 2023; L. A. Boogaard et al. 2024; S. Gillman et al. 2024; S. Bodansky et al. 2025; J. A. Hodge et al. 2025; R. Ikeda et al. 2025; F.-Y. Liu et al. 2026). However, existing samples remain heterogeneous and limited in size. A systematic census of rest-frame optical spectra for ALMA-selected galaxies spanning a broad range of redshifts and IR luminosities is still lacking.

This paper presents a first census of rest-frame optical to NIR JWST/NIRSpec spectra for 16 ALMA flux-limited dust continuum sources in the GOODS-S/HUDF field at $z_{\rm spec} = 1$–4 with IR luminosity spanning $\log(L_{\rm IR}/L_\odot) \sim 11$–$13$. We integrate these datasets to examine their rest-frame optical spectral features, ISM conditions, and origins of the dust continuum.

The structure of this paper is as follows. Section 2 describes our sample and datasets. Section 3 shows our analysis of the spectroscopic and photometric data, including emission-line flux measurements and SED fitting. Section 4 presents the results and the physical properties of the dust-continuum sources. In Section 5, we discuss the implications of these results. Section 6 summarizes our main findings. Throughout this paper, we assume a G. Chabrier (2003) ini-

tial mass function and a flat ΛCDM cosmology with $H_0 = 67.7$ km s^{-1} Mpc^{-1}, $\Omega_m = 0.31$, and $\Omega_\Lambda = 0.69$ (Planck Collaboration et al. 2020). We adopt a solar metallicity of $12 + \log(\mathrm{O/H}) = 8.69$ (M. Asplund et al. 2009). All magnitudes are in the AB system (J. B. Oke & J. E. Gunn 1983).

2. SAMPLE AND DATA

In this section, we describe the galaxy sample and the multi-wavelength datasets used in this study. Table 1 summarizes the sample and several key measurements from the literature, including dust-continuum flux densities ($S_{1.2\,\mathrm{mm}}$ and/or $S_{1.3\,\mathrm{mm}}$), IR luminosities (L_{IR}), X-ray luminosities (L_{X}), and molecular gas masses estimated from CO lines ($M_{\mathrm{mol,\,CO}}$).

2.1. *Galaxy Sample*

We compile ALMA flux-limited dust continuum sources in the HUDF. We adopt the sources detected in the HUDF survey (J. S. Dunlop et al. 2017) and the ALMA Spectroscopic Survey in the Hubble Ultra Deep Field Large Program (ASPECS-LP; M. Aravena et al. 2020) as the parent sample (38 sources in total). The rms depths of the HUDF survey and the ASPECS-LP are $S_{1.3\,\mathrm{mm}} = 30$ μJy beam^{-1} (J. S. Dunlop et al. 2017) and $S_{1.2\,\mathrm{mm}} = 9.3$ μJy beam^{-1} (M. Aravena et al. 2020), respectively. The detection procedures are summarized in J. S. Dunlop et al. (2017) and M. Aravena et al. (2020).

From this parent sample, we focus on 16 ALMA sources observed with the JWST/NIRSpec micro-shutter assembly (MSA) (hereafter, the UDF+ASPECS sample). Figure 1 shows the relation between the IR luminosities and redshift of the sample (red: UDF+ASPECS sample). The IR luminosities in this paper are taken from the literature (J. S. Dunlop et al. 2017; Y. Ueda et al. 2018; M. Aravena et al. 2020) and summarized in Table 1. The resulting UDF+ASPECS sample covers a wide redshift (z = 1–4) and IR luminosity range ($\log(L_{\mathrm{IR}}/L_\odot)$ = 11–13). For comparison, we also show other dusty galaxies, including local ($z < 0.5$) ultra luminous infrared galaxies (ULIRGs), the LABOCA Extended Chandra Deep Field South Survey (ALESS; J. A. Hodge et al. 2013; E. da Cunha et al. 2015), the Reionization Era Bright Emission Line Survey (REBELS; R. J. Bouwens et al. 2022), JWST/NIRCam dark galaxies (F. Sun et al. 2025), and other bright SMGs (SPT0311-58: e.g., D. P. Marrone et al. 2018, HFLS3: e.g., D. A. Riechers et al. 2013, HZ10: e.g., P. L. Capak et al. 2015, SPT0418-47: e.g., J. Cathey et al. 2024).

Figure 2 shows the sky distribution of the dust-continuum sources. Figure 3 presents the relation between the UV absolute magnitude (M_{UV}) and the 1 mm flux density ($S_{1\,\mathrm{mm}}$). M_{UV} is calculated by following Y. Xu et al. (2025) using the photometry described in Section 2.2.2. To obtain the magnitude, we use the photometry of the filter whose central wavelength is closest to the rest-frame wavelength of 1500 Å in the HST+JWST photometric catalog used in this study (see Section 2.2). In Figure 3, we compare the full dust-continuum sample reported by J. S. Dunlop et al. (2017) and M. Aravena et al. (2020) with the subset observed by NIRSpec (UDF+ASPECS sample). We find no clear trend between M_{UV} and $S_{1\,\mathrm{mm}}$ within the UDF+ASPECS sample. Sections 2.2 and 2.3 describe the details of the data and cross-matching procedures.

2.2. *UV to Infrared Data*

2.2.1. *Spectroscopy*

For the spectroscopic data of the UDF+ASPECS sample, we use publicly available NIRSpec-MSA medium-resolution grating data ($R \sim 1000$) from the JWST Advanced Deep Extragalactic Survey (JADES; D. J. Eisenstein et al. 2023; M. J. Rieke et al. 2023a; F. D'Eugenio et al. 2025; D. J. Eisenstein et al. 2025; E. Curtis-Lake et al. 2025; J. Scholtz et al. 2025) data release (DR) 4 (E. Curtis-Lake et al. 2025; J. Scholtz et al. 2025) and the Systematic Mid-Infrared Instrument Legacy Extragalactic Survey (SMILES; S. Alberts et al. 2024; G. H. Rieke et al. 2024; Y. Zhu et al. 2025) DR2 (Y. Zhu et al. 2025).

The JADES DR4 provides the NIRSpec-MSA spectra for 5190 sources in the GOODS field. The observations were conducted with a low-dispersion prism ($R \sim 100$), three medium-resolution gratings ($R \sim 1000$), and, for a subset, the higher-resolution G395H grating ($R \sim 2700$). From the JADES DR4, we use the medium-resolution grating data that cover 1–5 μm. The SMILES DR2 provides NIRSpec-MSA medium-resolution grating spectra for 166 galaxies at $0 < z < 7.5$ in the HUDF. The observations and reduction processes are described in E. Curtis-Lake et al. (2025); J. Scholtz et al. (2025) and Y. Zhu et al. (2025) for JADES and SMILES, respectively. We use the publicly released reduced spectra in our analysis.

We cross-match NIRSpec-MSA spectra to ALMA sources using a 0.″5 radius. The matched source IDs are listed in Table 1. When both JADES and SMILES spectra are available, we use the spectrum that covers more of the key diagnostic lines (Hβ, [O III], Hα, [N II], and [S II]). Table 2 includes a flag indicating whether the adopted spectrum is from JADES or SMILES. We note that UDF10 shows a 0.″54 offset between the JWST counterpart and the dust-continuum peak (see Figure 7).

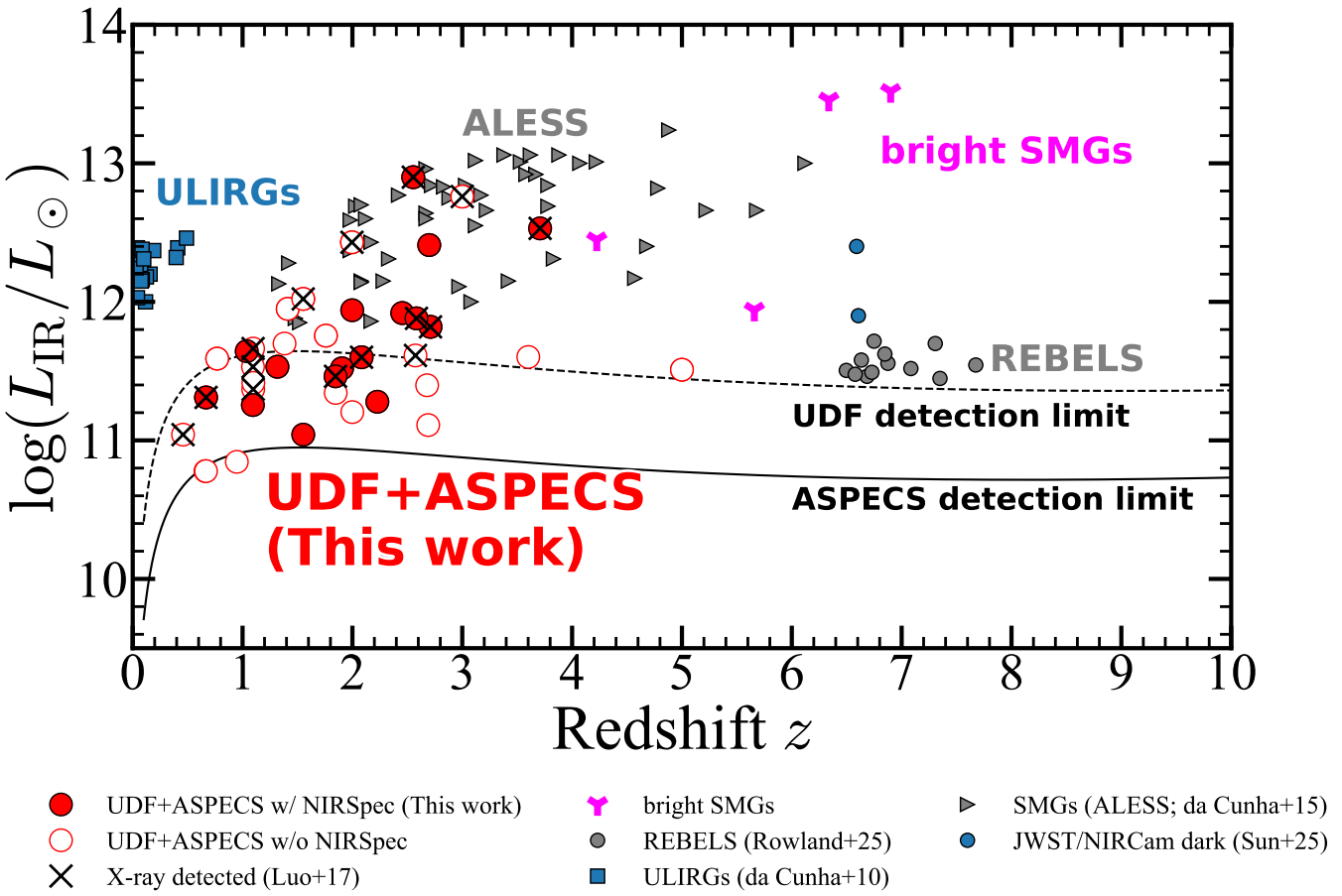

Figure 1. Relation between IR luminosity and redshift. Dust-continuum sources in HUDF are shown as open red circles (UDF: J. S. Dunlop et al. 2017; ASPECS: M. Aravena et al. 2020). Filled red circles indicate ALMA sources with JWST/NIRSpec (UDF+ASPECS sample in this study). The black crosses mark X-ray detections (B. Luo et al. 2017). Comparison samples are local ULIRGs at $z < 0.5$ (blue squares; E. da Cunha et al. 2010), ALESS (gray triangles; J. A. Hodge et al. 2013; E. da Cunha et al. 2015), JWST/NIRCam dark galaxies at $z = 6.6$ (blue circles; F. Sun et al. 2025), and REBELS (gray circles; R. J. Bouwens et al. 2022; L. E. Rowland et al. 2025). Some high-redshift bright SMGs are also highlighted as magenta (SPT0311-58: e.g., D. P. Marrone et al. 2018, HFLS3: e.g., D. A. Riechers et al. 2013, HZ10: e.g., P. L. Capak et al. 2015, SPT0418-47: e.g., J. Cathey et al. 2024). The black solid and dotted curves show the $L_{\rm IR}$ corresponding to the ASPECS ($S_{1.2\,\rm mm} > 0.03$ mJy; 3.3σ) and HUDF ($S_{1.3\,\rm mm} > 0.12$ mJy; 3.5σ) detection limits, respectively, assuming dust temperature of $T_{\rm dust} = 40$ K and emissivity index of $\beta_{\rm IR} = 1.5$.

We treat these as the same physical source and proceed with our analysis under this assumption, as J. S. Dunlop et al. (2017). UDF12 has spectra in JADES DR4, but these spectra lack emission lines or continuum, and no counterparts at the slit position. We exclude UDF12 from our final sample. UDF12 is originally reported to be a photometric redshift of $z_{\rm phot} = 5.0$ (J. S. Dunlop et al. 2017).

2.2.2. *Photometry*

For the rest-frame UV–optical photometry of the UDF+ASPECS sample, we use the public JADES DR2 photometric catalog (hereafter, the JADES photometric catalog; D. J. Eisenstein et al. 2025). The JADES photometric catalog provides the HST and JWST Near Infrared Camera (NIRCam; M. J. Rieke et al. 2023b) imaging in the GOODS-S/HUDF and incorporates the NIRCam medium-band data from the JWST Extragalactic Medium-band Survey (JEMS; C. C. Williams et al. 2023). We use the eight HST broadbands (Advanced Camera for Surveys F435W, F606W, F775W, F814W; Wide Field Camera 3 (WFC3) F105W, F125W, F140W, F160W) and 13 NIRCam broad and mediumbands, from F090W to F444W (F090W, F115W, F182M, F200W, F210M, F277W, F335M, F356W, F410M, F430M, F444W, F460M, F480M). The details

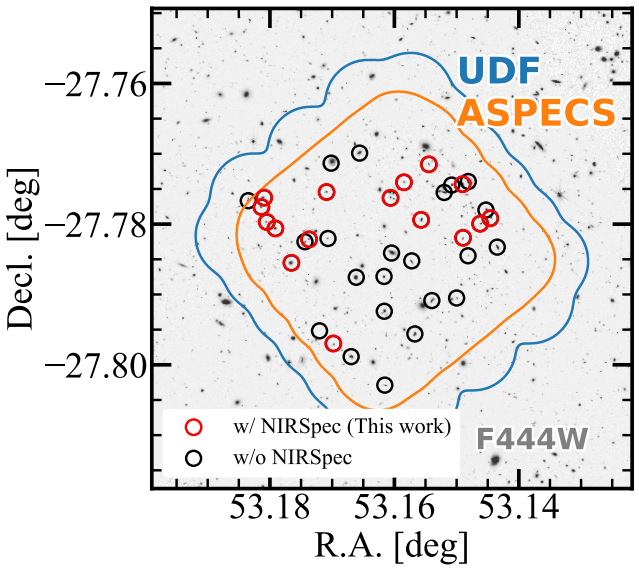

Figure 2. UDF (J. S. Dunlop et al. 2017) and ASPECS (M. Aravena et al. 2020) sky regions and the dust continuum source positions overlaid on the JWST/NIRCam F444W image. The blue and orange regions represent the survey areas of UDF and ASPECS, respectively. ALMA dust-continuum sources reported in the UDF and the ASPECS are shown as black open circles. The red open circles indicate the UDF or ASPECS sources with JWST/NIRSpec (UDF+ASPECS sample in this study).

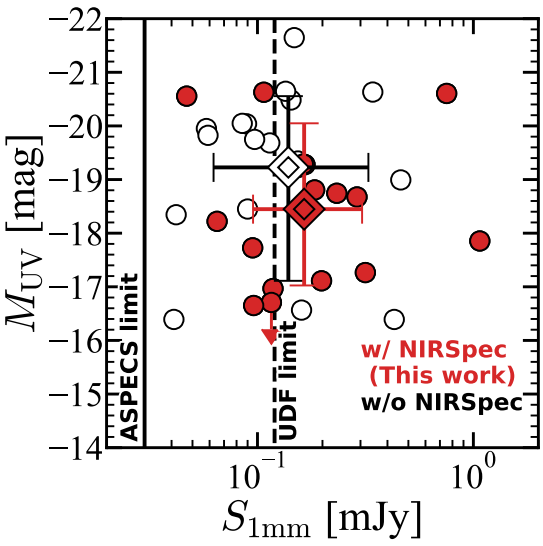

Figure 3. Relation between UV absolute magnitude ($M_{\rm UV}$) and 1 mm flux density ($S_{\rm 1\,mm}$). Dust-continuum sources reported in the UDF survey (J. S. Dunlop et al. 2017) and the ASPECS survey (M. Aravena et al. 2020) are shown as open circles (parent sample). Filled red circles indicate the sources with JWST/NIRSpec in the parent sample (UDF+ASPECS sample). If sources are detected in both ASPECS (1.2 mm) and UDF (1.3 mm), we plot the 1-mm flux density reported in the ASPECS (M. Aravena et al. 2020). Sources with non-detections in the rest-frame UV are shown as 3σ lower limits on $M_{\rm UV}$ as arrows. The black and red double diamonds show the medians for the parent sample and the UDF+ASPECS sample, respectively. The associated error bars indicate the 16th–84th percentile ranges. The black solid and dotted lines show the ASPECS ($S_{\rm 1.2\,mm} > 0.03$ mJy; 3.3σ) and UDF ($S_{\rm 1.3\,mm} > 0.12$ mJy; 3.5σ) detection limits, respectively.

of the image reduction and catalog construction are described in M. J. Rieke et al. (2023a) and D. J. Eisenstein et al. (2025).

To extend our wavelength coverage into the mid-infrared, we complement the JADES photometric catalog together with the SMILES DR1 photometric catalog, which provides JWST/Mid-Infrared Instrument (MIRI; P. Bouchet et al. 2015; G. H. Rieke et al. 2015; G. S. Wright et al. 2023) broadband imaging in the GOODS-S (see S. Alberts et al. 2024 for details). From this catalog, we use the eight MIRI broadbands from F560W to F2550W (F560W, F770W, F1000W, F1280W, F1500W, F1800W, F2100W, F2550W).

For both catalogs, we use the 2.5×-scaled Kron-aperture fluxes measured on raw-resolution images that are not PSF-matched. We adopt the associated random-aperture uncertainties provided in the catalogs as flux uncertainties. We do not correct the photometry for Galactic extinction. The expected extinction in the GOODS-S/HUDF is very small (typically $E(B-V) \lesssim 0.01$; e.g., E. F. Schlafly & D. P. Finkbeiner 2011, see also, E. Iani et al. 2024 for the correction factors of the NIRCam and MIRI bands). Its impact on our results is negligible.

We also utilize Herschel (G. L. Pilbratt et al. 2010) photometry from the FourStar Galaxy Evolution Survey (ZFOURGE) catalog (C. M. S. Straatman et al. 2016). We use the Herschel/Photodetector Array Camera and Spectrometer (PACS; A. Poglitsch et al. 2010) green (100 μm) and red (160 μm) band data to constrain the shorter wavelength dust continuum.

We associate these photometric catalogs with the ALMA dust-continuum sources by position. Starting from the ALMA continuum peak coordinates reported by J. S. Dunlop et al. (2017) and M. Aravena et al. (2020), we search for NIRCam and MIRI counterparts (Herschel counterparts) within a radius of 0.″5 (1.″0). All sources with NIRSpec data are cross-matched with NIRCam and MIRI photometry. The matched catalog IDs are listed in Table 1. These data are used for the SED fitting described in Section 3.2.

2.3. *X-ray Data*

In the GOODS-S field, ultra-deep Chandra observations have been accumulated over the past two decades (e.g., R. Giacconi et al. 2002; B. D. Lehmer et al. 2005; Y. Q. Xue et al. 2011; B. Luo et al. 2017). For the UDF+ASPECS sample, we make use of the Chandra Deep Field-South (CDF-S) 7 Ms source catalog presented by B. Luo et al. (2017) (see also Y. Ueda et al. 2018). We use these X-ray detections to identify AGNs among our dust-continuum sources (Section 4.2). We cross-match the 16 ALMA sources with JWST/NIRSpec spectra (UDF+ASPECS sample) to the CDF-S 7 Ms catalog within 1″, yielding seven matches. The CDF-S 7 Ms source catalog (B. Luo et al. 2017) provides absorption-corrected 0.5–7 keV X-ray luminosities. We summarize the corresponding source IDs (CID) and X-ray luminosities in Table 1.

3. ANALYSIS

3.1. *Emission-line Fitting and Flux Measurements*

We measure the key optical emission-line fluxes of Hβ, [O III]$\lambda\lambda$4959, 5007, Hα, [N II]$\lambda\lambda$6548, 6584, and [S II]$\lambda\lambda$6717, 6731 using the JWST/NIRSpec-MSA spectra. Emission-line fluxes are derived by least-squares fitting of Gaussian profiles and a linear continuum, implemented with the `scipy.optimize` package (P. Virtanen et al. 2020). We use the noise spectrum to weight the fit. In the Gaussian fitting, we generally model each emission line with a single Gaussian profile.

For each spectrum, we simultaneously fit the main nebular emission lines with Gaussians. Hβ and [O III]$\lambda\lambda$4959, 5007 are fit together with a common line width and redshift, and we fix the flux ratio $f_{[\mathrm{O\,III}]\lambda5007}/f_{[\mathrm{O\,III}]\lambda4959} = 2.98$ (P. J. Storey & C. J. Zeippen 2000) to reduce the number of free parameters. Likewise, Hα, [N II]$\lambda\lambda$6548, 6584, and [S II]$\lambda\lambda$6717, 6731 are fit simultaneously with a common line width and redshift, and fixing the flux ratio $f_{[\mathrm{N\,II}]\lambda6584}/f_{[\mathrm{N\,II}]\lambda6548} = 2.94$.

We constrain the Gaussian width to be larger than the instrumental broadening, assuming spectral resolutions of $R = 1000$ for the medium-resolution NIRSpec-MSA. The velocity dispersion is then calculated assuming $\sigma_{\mathrm{int}} = \sqrt{\sigma_{\mathrm{obs}}^2 - \sigma_{\mathrm{inst}}^2}$, where σ_{int}, σ_{obs}, and σ_{inst} are intrinsic, observed, and instrumental dispersions, respectively.

When the Balmer lines (e.g., Hα) show clear broad emission, we fit them with the sum of narrow and broad Gaussian components, while tying the redshift and velocity dispersion of the narrow components across all lines. Additionally, if broad components are also present in non-Balmer lines, we also fit an alternative model that includes both narrow and broad Gaussian components for all lines. To assess whether broad components are warranted, we use the Akaike Information Criterion (AIC; H. Akaike 1974):

$$\mathrm{AIC} = -2\ln(L) + 2k, \tag{1}$$

where L is the maximum likelihood and k is the number of free parameters. We adopt the model including broad components when $\Delta\mathrm{AIC} \equiv \mathrm{AIC}_{\mathrm{without\ broad}} - \mathrm{AIC}_{\mathrm{with\ broad}} > 20$.

Unless otherwise noted, we adopt the best-fit redshift from the Hα+[N II]+[S II] narrow lines as the source redshift throughout this paper (see Table 1). For sources without Hα coverage or detection, we use the redshift of the Hβ+[O III] fit instead.

Flux uncertainties are estimated by summing in quadrature the errors of the spectral bins within a wavelength interval of 2 × FWHM (full width at half-maximum) centered on the peak of the best-fit Gaussian profile. All rest-frame wavelengths are quoted on the vacuum wavelength scale (e.g., 5008.240 Å for [O III]λ5007), although we follow the long-standing nomenclature based on their air wavelengths. We summarize the emission-line measurements in Table 2. The flux measurements are broadly consistent with the JADES and SMILES emission-line flux catalog (E. Curtis-Lake et al. 2025; J. Scholtz et al. 2025; Y. Zhu et al. 2025).

3.2. *SED Fitting*

One strength of the UDF+ASPECS sample is the rich infrared to FIR photometry covered by JWST/MIRI, Herschel, and ALMA. These data constrain the dust-obscured star formation. We perform SED fitting with the Code Investigating GALaxy Emission (CIGALE version 2025.0; D. Burgarella et al. 2005; S. Noll et al. 2009; M. Boquien et al. 2019; G. Yang et al. 2020, 2022) to derive stellar masses and star formation rates (SFR) of the UDF+ASPECS sample.

We use JADES HST+NIRCam photometry and SMILES MIRI photometry (Section 2.2.2). We also include the Herschel photometry from the ZFOURGE catalog and the ALMA dust continuum measurements reported in J. S. Dunlop et al. (2017) and M. Aravena et al. (2020) (see Section 2.2.2). CIGALE computes model SEDs in an energy-conserving manner and derives physical properties as likelihood-weighted means over the full model grid (a Bayesian-like approach). The SED-fitting configuration is summarized below, and Appendix A lists the full set of parameters.

We adopt a delayed star-formation history (SFH) with an additional recent instantaneous variation in the SFR

Table 1. Far-infrared and X-Ray Properties of the UDF+ASPECS Sources.

ID (UDF)	ID (ASPECS)	ID (NIRSpec)	ID (NIRCam)	ID (MIRI)	CID	R.A. (J2000)	Decl. (J2000)	Redshift	$S_{1.3\,\mathrm{mm}}$ (μJy)	$S_{1.2\,\mathrm{mm}}$ (μJy)	$\log L_{\mathrm{IR}}$ ($L_\odot$)	$\log L_{\mathrm{X}}$ (erg s^{-1})	$M_{\mathrm{mol,\,CO}}$ ($10^{10}\,M_\odot$)
(1)	(2)	(3)	(4)	(5)	(6)	(7)	(8)	(9)	(10)	(11)	(12)	(13)	(14)
UDF2	C06	···	208820	1257	···	53.18137	−27.77757	2.697	996±87	1071±47	$12.41^{+0.10\,a}_{-0.10}$	···	11.0±1.3
UDF3	C01	14279	209117	1271	718	53.16062	−27.77627	2.543	863±84	752±24	$12.90^{+0.04\,a}_{-0.05}$	42.7	13.3±0.5
UDF4	C04	209357	209357	1284	···	53.17090	−27.77544	2.453	303±46	316±12	$11.92^{+0.13\,a}_{-0.16}$	···	5.0±0.5
UDF7	C11	···	208030	1231	797	53.18051	−27.77970	2.694	231±48	289±21	$11.82^{+0.20\,a}_{-0.19}$	42.6	···
UDF9	···	209108	209108	1272	799	53.18092	−27.77624	0.668	198±39	···	$11.31^{+0.48\,b}_{-0.48}$	40.9	···
UDF10	···	50039680	203108	1014	756	53.16981	−27.79697	2.084	184±46	···	$11.60^{+0.22\,b}_{-0.22}$	42.4	···
UDF13	C07	51236	208000	1225	655	53.14622	−27.77994	2.583	174±45	233±12	$11.88^{+0.05\,a}_{-0.07}$	42.4	···
UDF15	···	10007444	124908	1200	···	53.14897	−27.78194	1.904	166±46	···	$11.52^{+0.31\,b}_{-0.31}$	···	···
UDF16	C15	···	206183	1156	···	53.17655	−27.78550	1.317	155±44	118±13	$11.53^{+0.05\,a}_{-0.05}$	···	4.7±0.4
···	C08	209777	209777	1305	715	53.15846	−27.77406	3.711	···	163±10	$12.53^{+0.17\,a}_{-0.05}$	43.7	···
···	C13	···	207739	1773	···	53.17912	−27.78061	1.038	···	116±16	$11.64^{+0.04\,a}_{-0.05}$	···	3.7±0.4
···	C14a	···	207227	1196	···	53.17371	−27.78217	1.997	···	96±10	$11.94^{+0.08\,a}_{-0.14}$	···	···
···	C18	208134	208134	1236	703	53.15571	−27.77939	1.846	···	107±16	$11.46^{+0.16\,a}_{-0.12}$	42.2	···
···	C20	···	209480	1301	···	53.14904	−27.77433	1.094	···	95±16	$11.26^{+0.07\,a}_{-0.05}$	···	···
···	C26	208267	208267	1237	···	53.14458	−27.77917	1.552	···	65±15	$11.04^{+0.13\,a}_{-0.09}$	···	···
···	C31	10008071	210730	1345	···	53.15446	−27.77150	2.227	···	47±12	$11.28^{+0.49\,a}_{-0.05}$	···	···

Note— Far-infrared properties. (1) UDF source ID (J. S. Dunlop et al. 2017); (2) ASPECS ID (M. Aravena et al. 2020); (3) JADES NIRSpec ID in the JADES DR4 spectroscopic catalog (E. Curtis-Lake et al. 2025; J. Scholtz et al. 2025); (4) NIRCam ID in JADES DR2 photometric catalog (D. J. Eisenstein et al. 2025); (5) MIRI ID in SMILES DR1 catalog (Y. Zhu et al. 2025); (6) Chandra source ID in the CDF-S 7 Ms source catalog (B. Luo et al. 2017); (7) and (8) ALMA source position (J2000) based on the dust continuum detection (J. S. Dunlop et al. 2017; M. Aravena et al. 2020); (9) redshift measured from JWST/NIRSpec spectra; (10) total flux densities at 1.3 mm (UDF; J. S. Dunlop et al. 2017); (11) total flux densities at 1.2 mm (ASPECS; M. Aravena et al. 2020); (12) infrared luminosity: ^{a} based on M. Aravena et al. (2020); ^{b} based on J. S. Dunlop et al. (2017); Y. Ueda et al. (2018); (13) absorption-corrected intrinsic 0.5–7.0 keV luminosity (B. Luo et al. 2017); (14) gas mass estimated from CO lines (M. Aravena et al. 2019, 2020).

Table 2. Rest-frame Optical Emission-line Flux Measurements.

ID	ID	NIRSpec ID	ID	Redshift	Hβ	[O III]	Hα	[N II]	[S II]		Flag
(UDF)	(ASPECS)	(JADES)	(MIRI)			λ5007		λ6584	λ6717	λ6731	
UDF2	C06	···	1257	2.697	10.1±2.5	20.9±2.4	55.0±1.5	30.3±1.4	12.9±1.3	9.2±1.2	S
UDF3	C01	14279	1271	2.543	69.0±4.6	100.1±4.1	289.7±3.6	74.3±2.6	34.0±2.2	26.6±2.1	J
UDF4	C04	209357	1284	2.453	18.5±2.7	14.9±2.5	117.6±2.2	59.5±1.8	16.8±1.3	17.7±1.4	S
UDF7	C11	···	1231	2.694	23.1±3.8	41.8±3.4	148.4±3.1	78.5±2.9	36.1±5.4	18.7±2.8	S
UDF9	···	209108	1272	0.668	37.7±11.9	$<$ 26.5	317.9±8.9	116.7±5.2	58.7±4.2	54.2±4.2	J
UDF10	···	50039680	1014	2.084	52.2±2.7	97.5±3.4	419.9±4.8	140.8±3.3	36.6±2.7	33.3±2.2	S
UDF13	C07	51236	1225	2.583	$<$ 7.4	9.0±2.2	76.3±1.9	80.3±1.9	14.1±1.5	13.0±1.4	J
UDF15	···	10007444	1200	1.904	17.9±1.5	44.6±2.0	89.7±1.6	13.7±1.3	14.0±1.2	11.5±1.2	J
UDF16	C15	···	1156	1.317	$<$ 6.1	$<$ 6.1	96.6±2.7	105.4±3.4	12.6±2.4	11.9±2.4	S
···	C08[a]	209777	1305	3.711	17.3±2.5	88.9±2.6	105.6±3.6	53.0±3.3	$<$ 5.6	7.5±1.7	J
···	C13	···	1773	1.038	8.8±2.5	$<$ 5.9	203.1±2.5	110.4±2.2	28.2±1.7	23.5±1.6	S
···	C14a	···	1196	1.997	$<$ 4.6	$<$ 4.8	44.2±1.6	32.1±1.5	11.8±1.4	13.2±1.4	S
···	C18	208134	1236	1.846	19.5±2.7	17.4±2.8	96.6±3.1	38.3±2.7	15.7±2.6	14.9±2.4	J
···	C20	···	1301	1.094	$<$ 18.5	$<$ 16.6	181.4±7.1	88.6±6.0	$<$ 17.0	$<$ 17.2	S
···	C26	208267	1237	1.552	30.8±2.0	21.8±1.9	229.6±3.5	67.8±3.0	35.1±2.9	23.7±2.6	J
···	C31	10008071	1345	2.227	89.6±2.3	396.9±3.7	359.4±2.9	35.4±1.6	39.8±1.4	30.9±1.5	S

NOTE— Emission-line flux measurements of NIRSpec medium-resolution data. The fluxes are not corrected for dust extinction and units of $10^{-19}\,\mathrm{erg\,s^{-1}\,cm^{-2}}$. Errors are the 1σ uncertainties. Upper limits are 3σ levels. The flag indicates which dataset is used for the emission-line flux measurements (J: slit-loss-corrected JADES DR4 spectra extracted with a 5 pixel aperture and 3-nod pattern; S: SMILES DR2 spectra without slit-loss correction; see Y. Zhu et al. 2025 for details of the SMILES spectra).

[a]: C08 shows the prominent broad Balmer lines. Only the narrow line fluxes are shown (Figure 8; see also I. Juodžbalis et al. 2025).

Table 3. Physical Properties of the UDF+ASPECS Sources.

ID (UDF)	ID (ASPECS)	$\log M_*$ ($M_\odot$)	$\log$ SFR ($M_\odot$ yr^{-1})	$E(B-V)$ (mag)	[S II]6717/6731	n_e([S II]) (cm^{-3})	12 + log(O/H) (N2) (S21)	12 + log(O/H) (N2) (C20)	BPT	X-ray	AGN
(1)	(2)	(3)	(4)	(5)	(6)	(7)	(8)	(9)	(10)	(11)	(12)
UDF2	C06	10.89±0.04	2.48±0.05	0.57±0.21	1.41±0.23	28^{+339}_{-28}	9.01	8.54	T	F	T
UDF3	C01	9.80±0.02	2.81±0.02	0.35±0.06	1.28±0.13	193^{+229}_{-168}	8.70	8.34	F	T	T
UDF4	C04	10.06±0.24	1.97±0.06	0.70±0.12	0.95±0.11	1014^{+544}_{-354}	8.97	8.52	T	F	T
UDF7	C11	10.63±0.12	1.37±0.54	0.71±0.14	1.92±0.40	< 494	8.99	8.53	T	T	T
UDF9	···	9.92±0.08	0.43±0.05	0.95±0.27	1.08±0.11	582^{+354}_{-247}	8.83	8.44	F	T	T
UDF10	···	10.12±0.09	1.20±0.17	0.90±0.05	1.10±0.11	541^{+316}_{-231}	8.80	8.41	T	T	T
UDF13	C07	10.77±0.02	1.38±0.09	> 1.12	1.08±0.17	584^{+567}_{-337}	···	8.71	T	T	T
UDF15	···	10.05±0.03	1.00±0.02	0.50±0.07	1.22±0.17	294^{+367}_{-239}	8.53	8.21	F	F	F
UDF16	C15	10.78±0.02	1.36±0.07	> 1.48	1.05±0.29	669^{+1550}_{-560}	···	8.72	T	F	T
···	C08[a]	10.86±0.03	2.09±0.02	0.67±0.13	···	···	8.96	8.52	T	T	T
···	C13	10.47±0.04	1.32±0.04	1.80±0.25	1.20±0.11	330^{+231}_{-175}	9.00	8.54	F	F	F
···	C14a	10.13±0.02	1.62±0.07	> 1.06	0.89±0.14	1262^{+1018}_{-550}	9.18	8.61	T	F	T
···	C18	10.51±0.05	1.51±0.04	0.49±0.12	1.05±0.24	669^{+1114}_{-489}	8.86	8.46	F	T	T
···	C20	10.64±0.04	0.89±0.05	> 1.08	···	···	8.95	8.51	F	F	F
···	C26	10.16±0.05	1.02±0.13	0.84±0.06	1.48±0.21	< 604	8.75	8.38	F	F	F
···	C31	9.80±0.06	1.60±0.03	0.31±0.02	1.29±0.08	188^{+123}_{-104}	8.40	8.10	F	F	F

Note— (1)–(2) source IDs; (3) stellar mass in units of solar mass from CIGALE SED fitting; (4) SFR averaged in recent 10 Myr in units of $M_\odot$ yr^{-1} from CIGALE SED fitting; (5) Dust extinction $E(B-V)$ derived from Hα/Hβ ratio (see Section 4.1). Lower limits correspond to the 3σ levels. (6) [S II] doublet ratio that is not corrected for the dust extinction; (7) electron density derived from [S II] doublet. Upper limits correspond to the 2σ levels; (8) and (9) metallicity derived from the N2 index with the calibrations of R. L. Sanders et al. (2021) (S21) and S. P. Carvalho et al. (2020) (C20), respectively; (10) BPT flag (T: above the G. Kauffmann et al. 2003 curve in the BPT diagram, F: below the G. Kauffmann et al. 2003 curve in the BPT diagram); (11) X-ray flag (T: X-ray detection, F: no X-ray detection; B. Luo et al. 2017); (12) AGN flag (T: X-ray detection or BPT diagram above G. Kauffmann et al. 2003 curve, F: non-AGN).

[a]: C08 shows broad components in [O III] and the Balmer lines (Figure 8). Because their contribution to the [S II] doublet may not be reliably separated, we conservatively do not report an electron density.

(L. Ciesla et al. 2017). Stellar emission is modeled with the simple stellar population (SSP) templates of G. Bruzual & S. Charlot (2003). Nebular emission is included using templates based on the photoionization models of A. K. Inoue (2011). Dust attenuation is described by a modified D. Calzetti et al. (2000) attenuation law allowing a steeper slope in UV (C. Leitherer et al. 2002). Dust emission is modeled with the THEMIS dust model (A. P. Jones et al. 2017). The AGN component is included with the SKIRTOR2016 module (M. Stalevski et al. 2012, 2016). In this analysis, three AGN parameters are treated as free: the average edge-on optical depth at 9.7 μm ($\tau_{9.7}$), the inclination angle (i), and the AGN fraction ($f_{\rm AGN}$).

We fix the redshift to the JWST/NIRSpec value (Section 3.1; Table 1). For the HST, JWST/NIRCam, and MIRI photometry, we adopt a 5% uncertainty floor to account for remaining systematic uncertainties (e.g., B. Robertson et al. 2024; A. Weibel et al. 2024). For bands with a signal-to-noise ratio (S/N) below three, we treat the measurements as non-detections and use the corresponding 3σ upper limits in the SED fitting.

Table 3 summarizes the stellar masses and SFRs of the UDF+ASPECS sample derived from the SED fitting. Figure 4 shows the SFR–stellar mass relation, together with some literature. The UDF+ASPECS sources are mainly on the star-forming main sequence at $z \sim 2$ (see also, e.g., J. S. Dunlop et al. 2017; D. Elbaz et al. 2018; M. Aravena et al. 2020). These results (stellar mass and SFR) are broadly consistent with previous estimates obtained without JWST photometry (e.g., J. S. Dunlop et al. 2017; M. Aravena et al. 2020). Figure 5 shows some examples of the SED fitting results: C08 and C13 as examples of an AGN and prominent polycyclic aromatic hydrocarbon (PAH) emission, respectively. We note that C08 shows a relatively large reduced χ^2 (= 5.0); however, this discrepancy is driven mainly by the mid-infrared photometry, which is likely dominated by AGN emission. The stellar mass is mainly constrained by the rest-frame optical–NIR, and the SFR by the FIR. Thus, these estimates are not strongly affected by the mid-infrared discrepancy. These SED results, especially PAH emission, are also discussed in Section 4.6.

4. RESULTS

4.1. *Morphology and Spectra*

Figures 6–8 show the NIRCam images and NIRSpec spectra of the sample. The left panels of Figure 6 show the $5'' \times 5''$ cutouts. Nearly half of the UDF+ASPECS sources show multiple clumps or tidal features in the rest-frame optical NIRCam images via visual inspection. Previous studies suggest the connection between galaxy mergers and SMGs, especially for bright SMGs (e.g., P. F. Hopkins et al. 2008). It is worth noting that not all of the sources show merger-like morphology, possibly because the UDF+ASPECS sample is fainter than typical bright-SMG samples. A subset of sources (e.g., UDF13, C08) shows compact morphology and X-ray detections, suggesting AGN activities (see also Section 4.2). These morphological features are also reported in other JWST imaging studies (e.g., L. A. Boogaard et al. 2024 for the ASPECS sources; J. A. Hodge et al. 2025 for ALESS sources; R. Ikeda et al. 2025 for SMGs at $3.5 < z < 4.5$; S. Gillman et al. 2024 for ALMA sources in the Cosmic Evolution Survey and UKIDSS Ultra-Deep Survey field; J. McKinney et al. 2025 and J. Ren et al. 2025 for SCUBA SMGs).

The middle and right panels of Figure 6 show the spectra around Hβ+[O III] and Hα+[N II]+[S II], respectively. All sources show detections (S/N > 3) of Hα, [N II], while shorter wavelength optical emission lines (Hβ and [O III]) are weak. We estimate the dust attenuation $E(B-V)$ from the Balmer decrement, assuming an electron density of $n_e = 100$ cm^{-3}, an electron

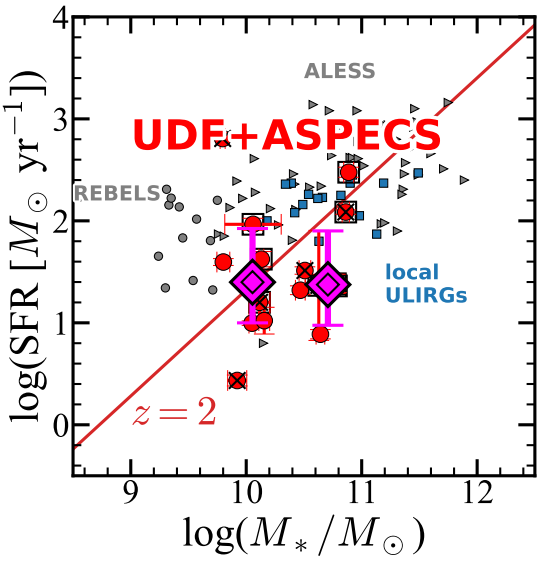

Figure 4. Relation between star formation rate (SFR) and stellar mass. The red circles show the UDF+ASPECS sample. The X-ray detected sources and BPT-AGN sources (Section 4.2) are shown as the black crosses and black squares, respectively. The magenta double diamonds with errorbars show the median and the 16th–84th percentiles of the UDF+ASPECS sample in two stellar-mass bins ($M_* < 10^{10.4}$ $M_\odot$ and $M_* > 10^{10.4}$ $M_\odot$). The red line shows the star formation main sequence at $z \sim 2$ (P. Santini et al. 2017). The ALESS (gray triangle; E. da Cunha et al. 2015), the REBELS (gray circle; L. E. Rowland et al. 2025), and the local ULIRGs (blue squares; E. da Cunha et al. 2010) are also shown.

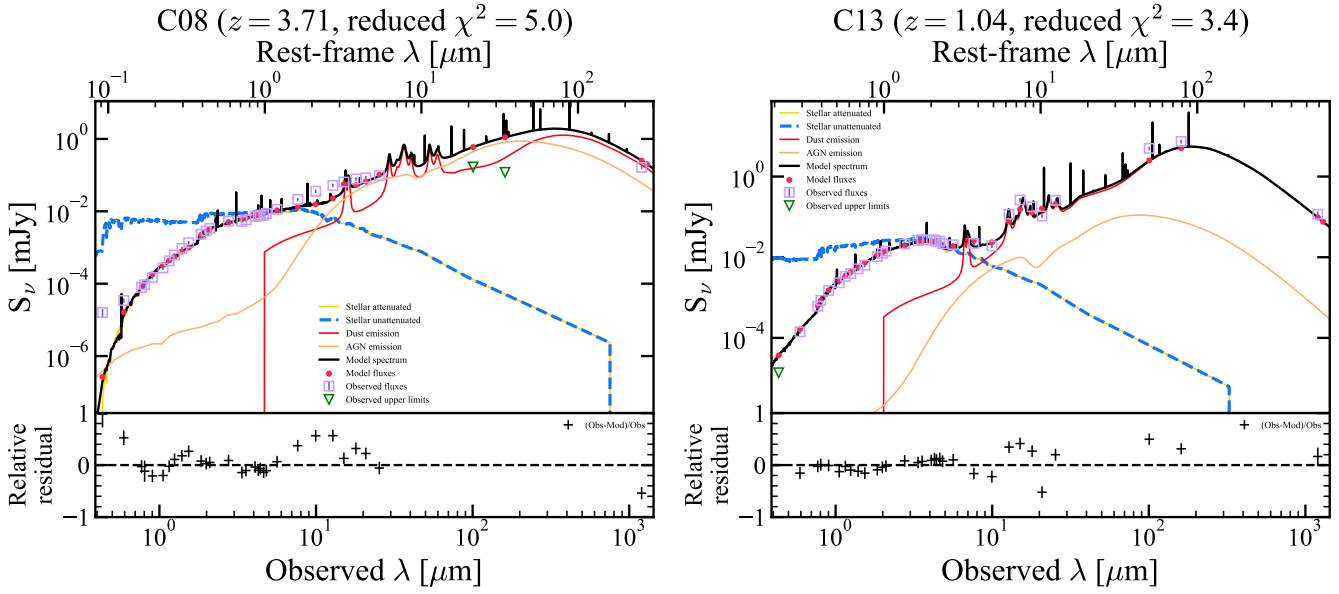

Figure 5. Some example SED-fitting results (left: C08 as an example of an AGN; right: C13 as prominent PAH emission). Top: The purple squares and green triangles indicate the observed photometry and the 3σ upper limits, respectively. The black curve shows the total best-fit SED, while the red, orange, blue-dashed, and yellow curves show the dust emission, AGN emission, dust-unattenuated, and dust-attenuated stellar emission, respectively. The reduced χ-square of the best-fit SED is indicated above the panels. Bottom: Relative residuals, $(F_{\rm obs} - F_{\rm model})/F_{\rm obs}$, between the observed photometry and the total best-fit SED. We note that AGN fractions ($f_{\rm AGN}$) of C08 and C13 are 0.50 ± 0.03 and 0.01 ± 0.02, respectively.

temperature of $T_e = 15,000$ K, case B recombination (D. E. Osterbrock & G. J. Ferland 2006), and D. Calzetti et al. (2000) law. We obtain $E(B-V) \sim 0.3$–1.8 for 12 sources. For the remaining four sources, the Hβ line is not detected, and 3σ lower limits of $E(B-V) \gtrsim 1.0$. We list their $E(B-V)$ in Table 3. We use these emission-line measurements in the following sections.

4.2. *AGN Signatures*

It is insightful to search for AGNs in these faint SMGs. We identify AGN candidates using three indicators: Chandra X-ray detections, the Baldwin–Phillips–Terlevich (BPT; J. A. Baldwin et al. 1981) diagram, and the presence of broad Balmer lines.

X-ray emission is a key signatures of AGN activity. As described in Section 2.3, we cross-matched the UDF+ASPECS sources to the Chandra CDF-S 7 Ms source catalog (B. Luo et al. 2017). We find seven matches among 16 sources (44%) within $1''$. We classify these X-ray–matched sources as AGNs (see also Y. Ueda et al. 2018).

Bringing the rest-optical spectra, we also constrain the AGN activity. Figure 9 shows the BPT diagram, with the demarcation curves separating star-forming galaxies and AGNs (L. J. Kewley et al. 2001; G. Kauffmann et al. 2003). Sources located above the curves are classified as AGN. In this study, we adopt G. Kauffmann et al. (2003) curve (black dashed curve) as a demarcation. If [O III] and Hβ are not detected, we indicate the sources as vertical lines. For these sources, we classify a galaxy as an AGN when $\log([\mathrm{N\,II}]\lambda6584/\mathrm{H}\alpha) > -0.2$ (e.g., A. M. Swinbank et al. 2004). When we calculate the line ratio of the BPT diagram, we correct the dust extinction using $E(B-V)$ obtained from the Hα/Hβ ratio if both lines are available (S/N > 3). We do not propagate the uncertainty in $E(B-V)$ into the line-ratio uncertainties.

From the BPT diagram, eight of 16 sources (50%) are classified as AGNs. Table 3 also lists the BPT-AGN classification for each source. Interestingly, some sources are classified as AGN in the BPT diagram, but have no X-ray counterparts (e.g., UDF2, UDF16). This might indicate that the X-rays of these sources are obscured by gas in the dust-sublimation region (S. Mizukoshi et al. 2024), and the observed X-ray could be weaker than the CDF-S detection limit. In addition, some sources lie between the G. Kauffmann et al. (2003) and L. J. Kewley et al. (2001) curves. This indicates a composite nature, where star formation alone may not account for the observed excitation. Such line ratios can be powered by a mixture of both star formation and AGN activity.

We note that the BPT locus and the demarcation curves may evolve with redshift (L. J. Kewley et al. 2013) because they depend on the ionizing radiation field and ISM conditions. In this study, we adopt the traditional G. Kauffmann et al. (2003) demarcation curve as

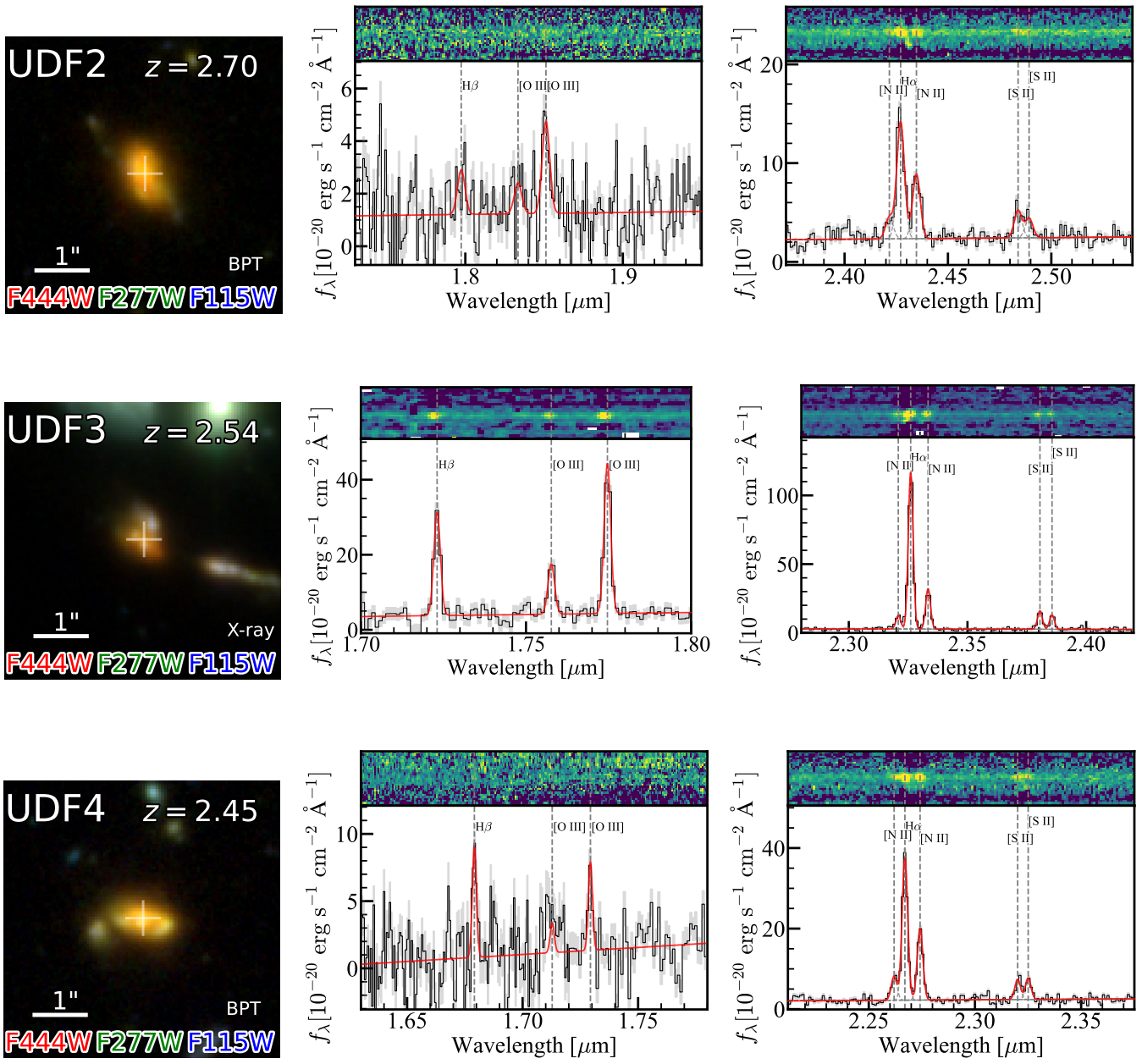

Figure 6. NIRCam images and NIRSpec spectra of UDF2, UDF3, and UDF4. Left: pseudocolor images ($5'' \times 5''$; blue: NIRCam F115W, green: NIRCam F277W, red: NIRCam F444W). The white cross shows the position of the dust continuum peak (J. S. Dunlop et al. 2017; M. Aravena et al. 2020). The bar in the bottom-left corner shows a $1''$ scale (8.3 kpc at $z = 2.5$). The marks 'X-ray' and/or 'BPT' present the X-ray detection and/or are classified as AGN in the BPT diagram using G. Kauffmann et al. (2003) curve. Middle: NIRSpec spectrum around the wavelength of Hβ and [O III]$\lambda\lambda$4959, 5007 emission lines. The top and the bottom panels show the two-dimensional spectrum and the one-dimensional spectrum, respectively. The black solid lines and gray shades show the observed spectrum and associated 1σ uncertainties, respectively. The red solid curves show the best-fit spectrum. Right: Same as in the middle panel but for Hα, [N II]$\lambda\lambda$6548, 6584, and [S II]$\lambda\lambda$6717, 6731 emission lines.

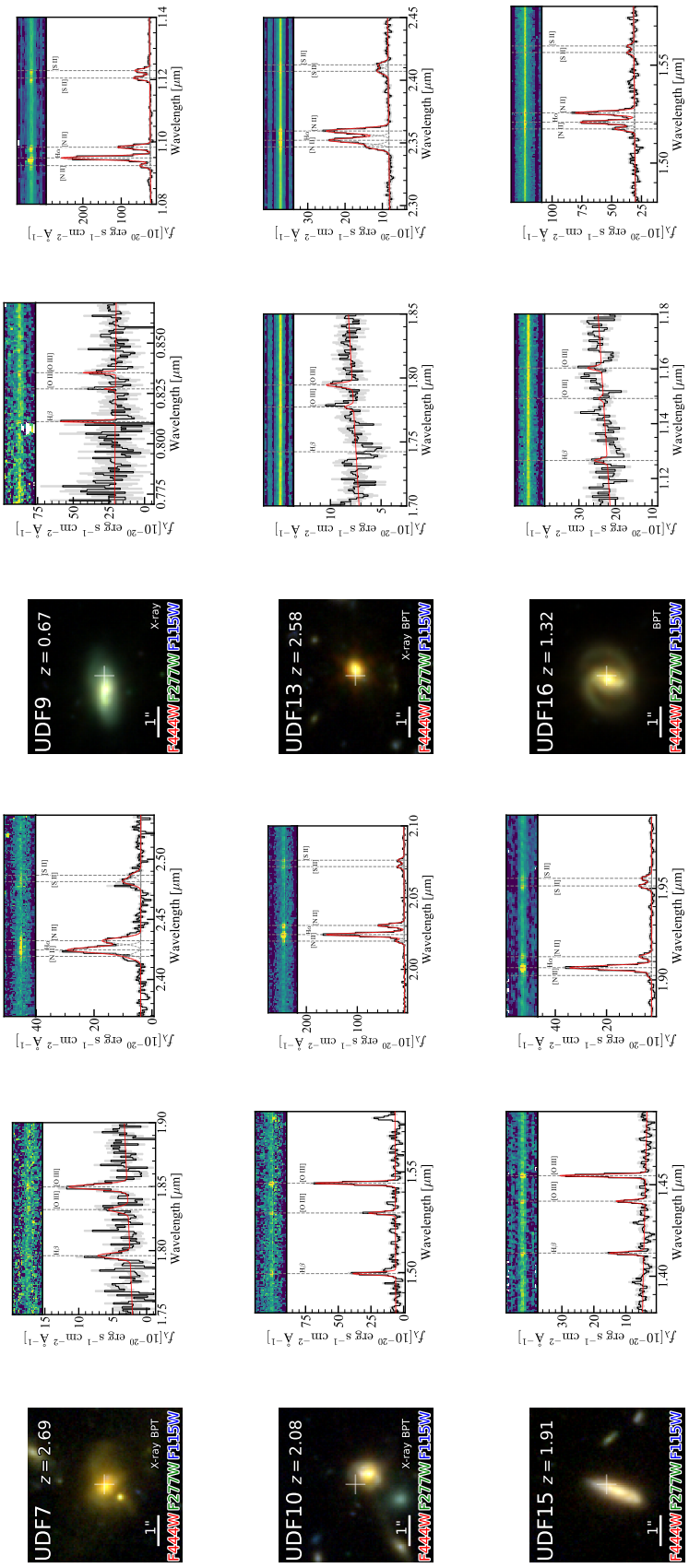

Figure 7. Same as in Figure 6 but for UDF7–UDF16.

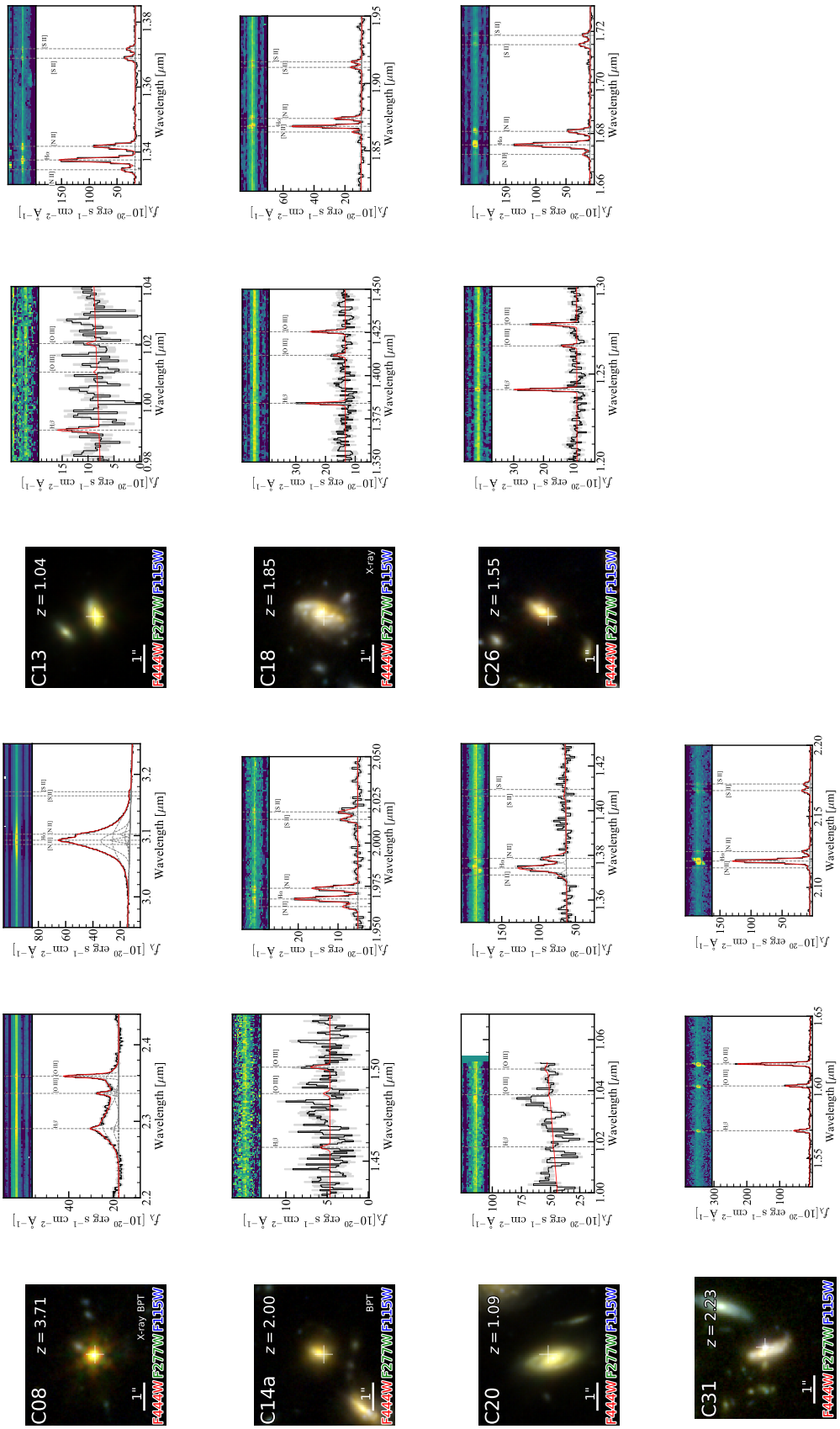

Figure 8. Same as in Figure 6 but for C08–C31.

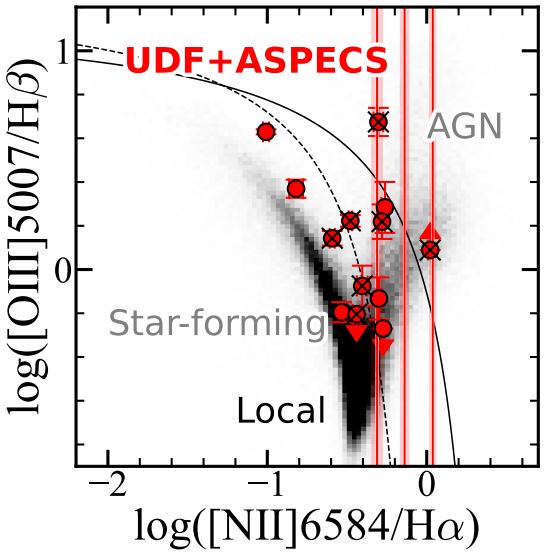

Figure 9. BPT diagram. The UDF+ASPECS sources are plotted as red circles or red lines. If neither [O III] nor Hβ is detected, we indicate the sources as vertical lines together with red shades indicating 1σ uncertainties. The black crosses indicate the X-ray detected sources. Two demarcation curves between star-forming galaxies and AGNs are shown as dashed (G. Kauffmann et al. 2003) and solid (L. J. Kewley et al. 2001) lines. The background gray scales show the distribution of the SDSS galaxies taken from the SDSS DR16 (R. Ahumada et al. 2020).

a criterion of AGN, following the previous studies (e.g., G. C. Jones et al. 2024).

Broad Balmer emission lines (FWHM $\gtrsim 1000$ km s^{-1}) with narrow forbidden lines also suggest that the broad component is powered by AGN activity, especially from the broad line region (e.g., R. Maiolino et al. 2024; J. E. Greene et al. 2024). In our sample, C08 ($z = 3.71$; Figure 8) shows broad Hα lines with FWHM $\sim 6500\,\mathrm{km\,s^{-1}}$ and narrow [O III] which is also reported in I. Juodžbalis et al. (2025) (object ID: JADES-GS-209777, Figure 1 of I. Juodžbalis et al. 2025). We therefore classify C08 as a type-1 AGN. I. Juodžbalis et al. (2025) estimate a black hole mass ($M_{\rm BH}$) of $\log(M_{\rm BH}/M_\odot) = 8.9 \pm 0.3$ from the broad Hα assuming the virial relation (A. E. Reines & M. Volonteri 2015). C08 also shows a compact morphology (Figure 8), an X-ray detection (CID: 715, B. Luo et al. 2017), and a BPT-AGN (the top-right outlier in Figure 9), further supporting the presence of AGN. Other sources do not show prominent broad Balmer components (FWHM $\gtrsim 1000\,\mathrm{km\,s^{-1}}$) with narrow [O III], indicating that other X-ray-selected and/or BPT-AGNs are type-2, and the broad line regions might be obscured.

UDF13 (X-ray detection, BPT-AGN, and compact) shows a broad Hα component with FWHM $= 1400 \pm 160$ km s^{-1} and ΔAIC $= 40$. However, [O III] lines are not detected with sufficient S/N, so we cannot exclude an outflow origin for the broad emission. Fitting the Hα+[N II]+[S II] complex with a model that includes both narrow emission and broad outflow components yields a better fit than a model only with narrow lines. Given these ambiguities, we do not further discuss UDF13 as a broad-line AGN. We briefly note that UDF13 (JADES ID: 208000) is also identified as a MIRI AGN candidate by J. Lyu et al. (2024) and G. H. Rieke et al. (2025).

It is worth noting that outflow and galaxy mergers can also broaden the line widths. If these mechanisms dominate the line width, we observe broad components in both permitted and forbidden lines. However, C08 has the broad component only in the permitted (Hα and Hβ) lines, suggesting that the broad components are powered by AGN activity.

In total, 11 out of 16 sources (69%) are classified as AGNs. Figure 10 summarizes the AGN fraction (identified via the BPT diagram and/or X-rays) as a function of stellar mass. In both stellar-mass bins ($\log(M_*/M_\odot) =$ 9.5–10.5 and 10.5–11.0), the AGN fraction exceeds 50% (56% and 86%, respectively). The high incidence of AGN signatures in X-rays and/or the BPT diagram is consistent with a scenario in which many of these systems host obscured AGNs (e.g., P. F. Hopkins et al. 2008). Y. Ueda et al. (2018) show the Chandra X-ray analysis for the UDF and ALMA twenty-six arcmin^2 survey of GOODS-S at one millimeter (ASAGAO; B. Hatsukade et al. 2018) sources. They also report the high AGN fraction for these samples, 38% for UDF and 67% for ASAGAO (see also, e.g., S. X. Wang et al. 2013). We further identify the AGNs that are missed in X-ray surveys and constrain their rest-frame optical properties. This result highlights the importance of a multi-wavelength approach to AGN diagnostics. We note that these extensive surveys have been conducted in other fields. For example, H. Umehata et al. (2015) reported $\sim$ 50% of SMGs in the SSA22 protocluster core host X-ray-luminous AGNs based on ALMA and Chandra.

We consider the detection limit of the broad Hα line in the JWST/NIRSpec spectra. We can assume a typical stellar mass of the UDF+ASPECS sample to be $\log(M_*/M_\odot) \sim 10.5$, and $M_*/M_{\rm BH} = 10^3$ (e.g., J. Kormendy & L. C. Ho 2013). This corresponds to the black hole mass of $\log(M_{\rm BH}/M_\odot) \sim 7.5$. Assuming a H$\alpha$ broad line width of FWHM $= 1500\,\mathrm{km\,s^{-1}}$ and the A. E. Reines & M. Volonteri (2015) relation, the corresponding Hα luminosity is $\sim 10^{42}$ erg s^{-1}. If there is no dust extinction, we detect the broad Hα component, fur-

ther supporting that the AGNs in the UDF+ASPECS sample are dust obscured.

For comparison, we estimate the AGN fraction for ALMA non-detected sources. We select sources observed with NIRSpec in the JADES DR4 and SMILES DR2 spectroscopic catalogs and in the ASPECS footprint. Following the same procedure as for the UDF+ASPECS sample, we classify AGN candidates using X-ray and BPT, based on the CDF-S 7 Ms catalog and emission-line fluxes reported in JADES DR4 or SMILES DR2 spectroscopic catalogs. Since robust stellar masses are not available for all sources in the parent sample, we estimate stellar masses from the F444W absolute magnitude ($M_{\rm F444W}$) using empirical calibration. F444W probes the rest-frame $\sim$ 1–2 μm at $z \sim 2$, and thus primarily traces the stellar continuum. We derive a linear relation between $M_{\rm F444W}$ and $\log(M_*/M_\odot)$ using the COSMOS-Web photometric catalog (C. M. Casey et al. 2023; M. Shuntov et al. 2025), which provides both photometry and stellar masses from the SED fitting. We select galaxies at $z = 1.5$–3.5 and $m_{\rm F444W} < 26$ from the catalog and fit a linear model in the ($M_{\rm F444W}$, $\log(M_*/M_\odot)$) plane. This calibration has a scatter of $\sim$ 0.3 dex. We then apply this linear relation to the galaxies at $z = 1.5$–3.5 to estimate their stellar masses. For sources at $z = 1.5$–3.5 and $\log(M_*/M_\odot) = 9.5$–10.5, we find an AGN fraction of $\sim 30\%$ (3/10; the black circle in Figure 10). We caution that the inferred AGN fraction for lower-mass galaxies is likely a lower limit. Due to the incompleteness of the Chandra X-ray and JWST/NIRSpec observations, we might miss the AGNs for fainter galaxies.

4.3. *Relation between [OIII] and X-Ray luminosity*

We compare the relation between the observed [O III]λ5007 luminosity and the intrinsic X-ray luminosity for the X-ray selected AGNs in our UDF+ASPECS sample with that for local X-ray AGNs. The [O III] emission lines can also trace narrow line regions, and comparison with their X-ray luminosities is insightful. Figure 11 shows the relation between the [O III] luminosity without dust-extinction correction and the absorption-corrected 0.5–7 keV X-ray luminosity. Relative to the local [O III]–X-ray relation from Y. Ueda et al. (2015), our sources show higher [O III] luminosities at a fixed X-ray luminosity by $\gtrsim$ 0.5 dex. For fair comparison, we plot the local AGNs in Y. Ueda et al. (2015) after converting the reported 2–10 keV X-ray luminosities to 0.5–7 keV luminosities assuming a photon index of $\Gamma = 1.8$. [O III] luminosities are estimated using slit-loss-corrected spectra provided in the JADES DR4 and SMILES DR2.

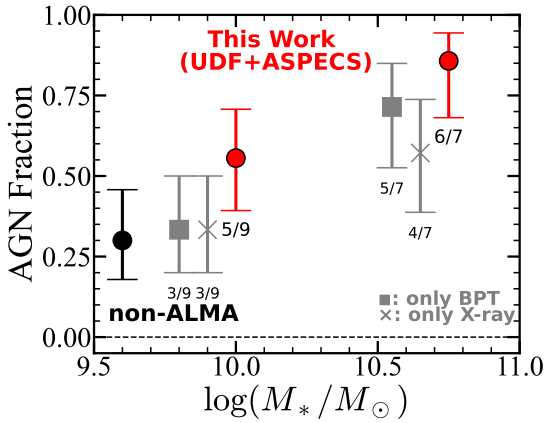

Figure 10. Fraction of sources classified as AGNs based on the BPT diagram and/or X-rays as a function of stellar mass. Red circles show the AGN fraction identified via the BPT diagram and/or X-rays, while gray squares and crosses show the fractions based on the BPT diagram only and X-rays only, respectively. Numbers below the plot show the AGN count over the total number of galaxies in each stellar-mass bin. Error bars indicate 1σ binomial uncertainties. The stellar mass bins are $\log(M_*/M_\odot) = 9.5$–10.5 and 10.5–11.0. For reference, ALMA non-detected sources ($\log(M_*/M_\odot) = 9.5$–10.5) at $z = 1.5$–3.5 are also indicated by a black circle. For clarity, the points are slightly offset along the x-axis.

Several effects could contribute to this offset. 1) Contamination from star formation. Star formation can contribute to the total [O III] flux and could lead to high [O III] luminosity. 2) Different bolometric correction. If these AGNs have larger X-ray bolometric corrections κ_X (ratio between bolometric luminosity and X-ray luminosity) than the nominal value (e.g., $\kappa_{0.5-8\,\rm keV} = 5$–$20$; J. R. Rigby et al. 2009; F. Duras et al. 2020), they would become [O III]-bright at a given X-ray luminosity compared to local AGNs (see also discussions in Y. Ueda et al. 2018). 3) Compton thick case. If the AGNs are Compton thick, we might observe X-rays dominated by scattered components. This could underestimate the X-ray luminosities even after the absorption correction.

4.4. *Gas-phase Metallicity*

Bringing the rest-optical emission lines, we estimate gas-phase metallicities for the dust continuum sources. Since the aural line [O III]λ4363 is not detected for those dust continuum sources, we do not use the direct method to estimate metallicity. We instead adopt commonly used strong line calibrations. In our galaxy sample, all sources have Hα and [N II] lines, and we utilize the N2 index ([N II]λ6584/Hα) as an indicator of metallicity.

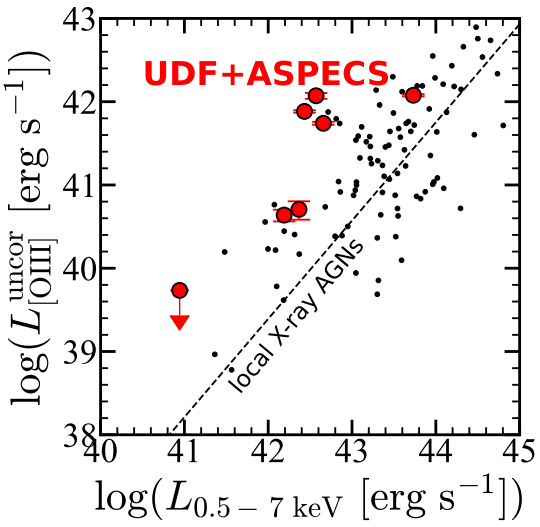

Figure 11. Correlation between the intrinsic X-ray luminosity in the 0.5–7 keV band and observed [O III]λ5007 luminosity. The red circles indicate the X-ray detected sources in the UDF+ASPECS sample. The black circles and dashed line show the local X-ray AGNs and their best-fit regression lines reported in Y. Ueda et al. (2015), respectively. For sources and best-fit line from Y. Ueda et al. (2015), we convert the reported 2–10 keV luminosities to 0.5–7 keV luminosities assuming a photon index of $\Gamma = 1.8$.

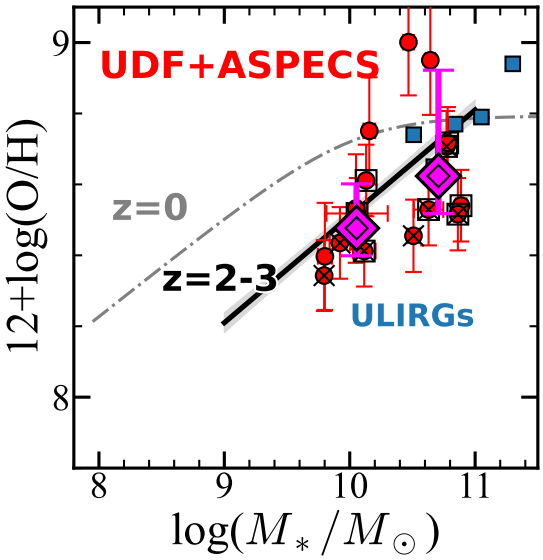

Figure 12. Relation between stellar mass and gas-phase metallicity. The red circles show the UDF+ASPECS sample. The black crosses and black squares show the X-ray AGN and BPT-AGN, respectively. The magenta double diamonds with errorbars show the median and the 16th–84th percentiles of the UDF+ASPECS sources in two stellar-mass bins ($M_* < 10^{10.4}\ M_\odot$ and $M_* > 10^{10.4}\ M_\odot$). The black solid line and the gray dot-dashed line show the relations of star-forming galaxies at $z = 2$–3 (R. L. Sanders et al. 2021) and $z = 0$ (M. Curti et al. 2020), respectively. The local ULIRGs are plotted as the blue squares (N. Chartab et al. 2022).

We use the N2 calibration presented in R. L. Sanders et al. (2021):

$$\log([\mathrm{N\,II}]\lambda6584/\mathrm{H}\alpha) = c_0 + c_1 x + c_2 x^2 + c_3 x^3, \quad (2)$$

where $x = 12 + \log(\mathrm{O/H}) - 8.69$ and $(c_0, c_1, c_2, c_3) = (-0.606, 1.28, -0.435, -0.485)$. This relation is calibrated using star-forming galaxies at $z \sim 0$ with the stellar mass range of $\log(M_*/M_\odot) = 9.0$–11.0. We note that R. L. Sanders et al. (2021) calibration is established using the star-forming galaxies, and removes AGNs from their sample, using X-ray detections and infrared properties (see Section 2.3 of R. L. Sanders et al. 2021).

To conservatively test the contribution from AGNs to the N2 index measurements, we also use the N2 index calibration presented in S. P. Carvalho et al. (2020). This is calibrated by the Seyfert 2 AGNs based on the Sloan Digital Sky Survey (SDSS; D. G. York et al. 2000):

$$Z/Z_\odot = a^{\log([\mathrm{N\,II}]\lambda6584/\mathrm{H}\alpha)} + b, \quad (3)$$

where $a = 4.01$, $b = -0.07$. N2 index uncertainties are propagated to the metallicity estimate. The systematic calibration uncertainties (0.15 dex for R. L. Sanders et al. 2021 and 0.10 dex for S. P. Carvalho et al. 2020) are also included in quadrature with the metallicity uncertainties, which dominate the total uncertainties. The results using R. L. Sanders et al. (2021) and S. P. Carvalho et al. (2020) calibrations are summarized in Table 3. Hereafter, if the sources have the AGN signatures (X-ray or BPT diagram; Section 4.2), we use the metallicity derived from the Seyfert 2 AGN calibration (S. P. Carvalho et al. 2020); otherwise, we use the star-forming galaxy calibration (R. L. Sanders et al. 2021).

Figure 12 shows the relation between gas-phase metallicity and stellar mass. The UDF+ASPECS sources (red circles) have metallicities in the range of 12+log(O/H) = 8.3–9.0 (i.e., 0.4–2$Z_\odot$). Compared to the mass metallicity relation at $z = 2$–3 (R. L. Sanders et al. 2021), the UDF+ASPECS sources have comparable metallicities and broadly follow the mass metallicity relation. Since the UDF+ASPECS dust continuum sources have high stellar masses ($\log(M_*/M_\odot) \gtrsim 10$), some sources reach nearly solar metallicities. We discuss implications from the metallicity for dusty galaxies in Section 5.

4.5. *Electron Density*

The electron density provides a useful diagnostic of the physical conditions of ISM (e.g., R. L. Sanders et al. 2016). We derive the electron densities of the dust-continuum sources from the [S II]$\lambda\lambda$6717, 6731 dou-

blet ratio when both lines are detected with S/N > 3. The medium-resolution grating data ($R \sim 1000$) are sufficient to resolve the [S II] doublet. We use the PyNeb (version 1.1.28; V. Luridiana et al. 2015) package `getTemDen` with the default PyNeb atomic datasets (S^+ transition probabilities from P. Rynkun et al. 2019 and S^+ collision strengths from S. S. Tayal & O. Zatsarinny 2010) to convert the observed ratios into electron densities. In these calculations, we assume an electron temperature of $T_e = 15{,}000$ K. Varying the assumed temperature within a plausible range (e.g., $T_e = 10{,}000$–$20{,}000$ K) does not affect the general trends discussed in this paper. When the observed [S II] doublet ratio falls beyond the low (high) density limits, we set the 2σ upper (lower) limits of the electron density. The uncertainties in the [S II] doublet ratio are propagated to the electron density uncertainties. The [S II] doublet ratio and electron densities are summarized in Table 3. The median value of the [S II] electron density of our sample is $n_e([\mathrm{S\,II}])_{\mathrm{med}} = 541$ cm^{-3}.

Figure 13 shows the [S II] electron densities as a function of redshift, stellar mass, SFR, and SFR surface density ($\Sigma_{\mathrm{SFR}}^{\mathrm{global}}$). In these figures, we also plot the results taken from the Assembly of Ultradeep Rest-optical Observations Revealing Astrophysics (AURORA; e.g., A. E. Shapley et al. 2025) survey for star-forming galaxies at $z = 1$–6 (gray squares; M. W. Topping et al. 2025). We first check the relation between the electron density and redshift of the sample (panel (a) of Figure 13). Compared to the redshift evolution presented by M. W. Topping et al. (2025) (black curve in panel (a) of Figure 13), the UDF+ASPECS sample shows high electron densities. To evaluate this trend, we compare the electron density with SFR (panel (b) of Figure 13). The UDF+ASPECS sources have $\log(\mathrm{SFR}\ [M_\odot\ \mathrm{yr}^{-1}]) \sim 1$–3. M. W. Topping et al. (2025) show the correlation between the electron density and SFR (black line), and the UDF+ASPECS sample aligns with this relation. Higher electron densities than those of the galaxies at similar redshifts can be explained by the higher SFR.

The relation between the electron density and stellar mass (panel (c) of Figure 13) is comparable to that of star-forming galaxies at similar redshifts reported by M. W. Topping et al. (2025). Our galaxy sample is biased toward massive systems ($\log(M_*/M_\odot) \gtrsim 10$) due to the selection effects associated with the ALMA dust-continuum detection.

The panel (d) of Figure 13 shows the relation between the electron density and surface SFR density. To obtain the surface SFR density for the UDF+ASPECS sources, we use the galaxy sizes presented in A. van der Wel et al. (2012). A. van der Wel et al. (2012) conduct global structural parameter measurements for the CANDELS survey using the GALFIT (C. Y. Peng et al. 2002) Sersic model fits of HST/WFC3 H_{160} images. The surface SFR density is calculated as $\Sigma_{\mathrm{SFR}}^{\mathrm{global}} = \mathrm{SFR}/(2\pi r_e^2)$. Here, r_e is a circularized effective radius, as $r_e = r\sqrt{b/a}$, where r is a half-light radius along the major axis, and b/a is an axis ratio from the Sersic model fitting. The SFR values are obtained from the SED fitting (Section 3.2). The UDF+ASPECS sources have surface SFR densities of $\log(\Sigma_{\mathrm{SFR}}^{\mathrm{global}}\ [M_\odot\ \mathrm{yr}^{-1}\ \mathrm{kpc}^{-2}]) \sim -1$–1 (see also W. Rujopakarn et al. 2016). Relative to the tentative Σ_{SFR}–n_e correlation reported by M. W. Topping et al. (2025) (black solid line; panel (d) of Figure 13), the UDF+ASPECS sources show electron densities that are consistent with the relation.

4.6. *PAH Emission*

PAH features (e.g., 3.3 μm, 6.2 μm, and 7.7 μm; e.g., A. G. G. M. Tielens 2008) fall within the JWST/MIRI wavelength coverage for the UDF+ASPECS sample and could provide an additional probe of dust conditions. As shown in Figure 5, MIRI photometry successfully traces the PAH emission lines ($\lambda_{\mathrm{obs}} \sim 10$–$20\,\mu$m). In the UDF+ASPECS sample, sources classified as AGN (e.g., UDF3 and C08; Figure 5) show weaker PAH features in their SEDs than those of the non-AGN sources (e.g., C13; Figure 5). This qualitative trend is consistent with scenarios in which intense AGN radiation fields suppress PAH emission (e.g., R. Genzel et al. 1998). A quantitative analysis of the PAH strengths of the ALMA sources is beyond the scope of this paper, and we defer to future studies (see also, e.g., J. S. Spilker et al. 2023; I. Shivaei et al. 2024; G. H. Rieke et al. 2025).

These studies can be extended to higher-redshift dusty galaxies with the proposed PRobe Infrared Mission for Astrophysics (PRIMA; J. Glenn et al. 2025). Its Far-Infrared Enhanced Survey Spectrometer (FIRESS; C. M. M. Bradford et al. 2025) will provide spectroscopic data over 24–235 μm, allowing us to trace PAH emission and other mid-/far-IR diagnostics over a wide redshift range ($z \gtrsim 1$) with spectroscopy.

4.7. *Dust Properties*

Comparing the dust masses of these faint SMGs with other physical properties, especially the metallicities newly constrained by JWST spectroscopy, provides insight into their nature. We estimate dust masses of the UDF sources reported in J. S. Dunlop et al. (2017) using the following modified black body:

$$M_{\mathrm{dust}} = \frac{D_{\mathrm{L}}^2 S_{\nu,\mathrm{obs}}}{(1+z)\kappa_{\mathrm{d}}(\nu_{\mathrm{rest}})[B_\nu(T_{\mathrm{dust}}) - B_\nu(T_{\mathrm{CMB}}(z))]}, \quad (4)$$

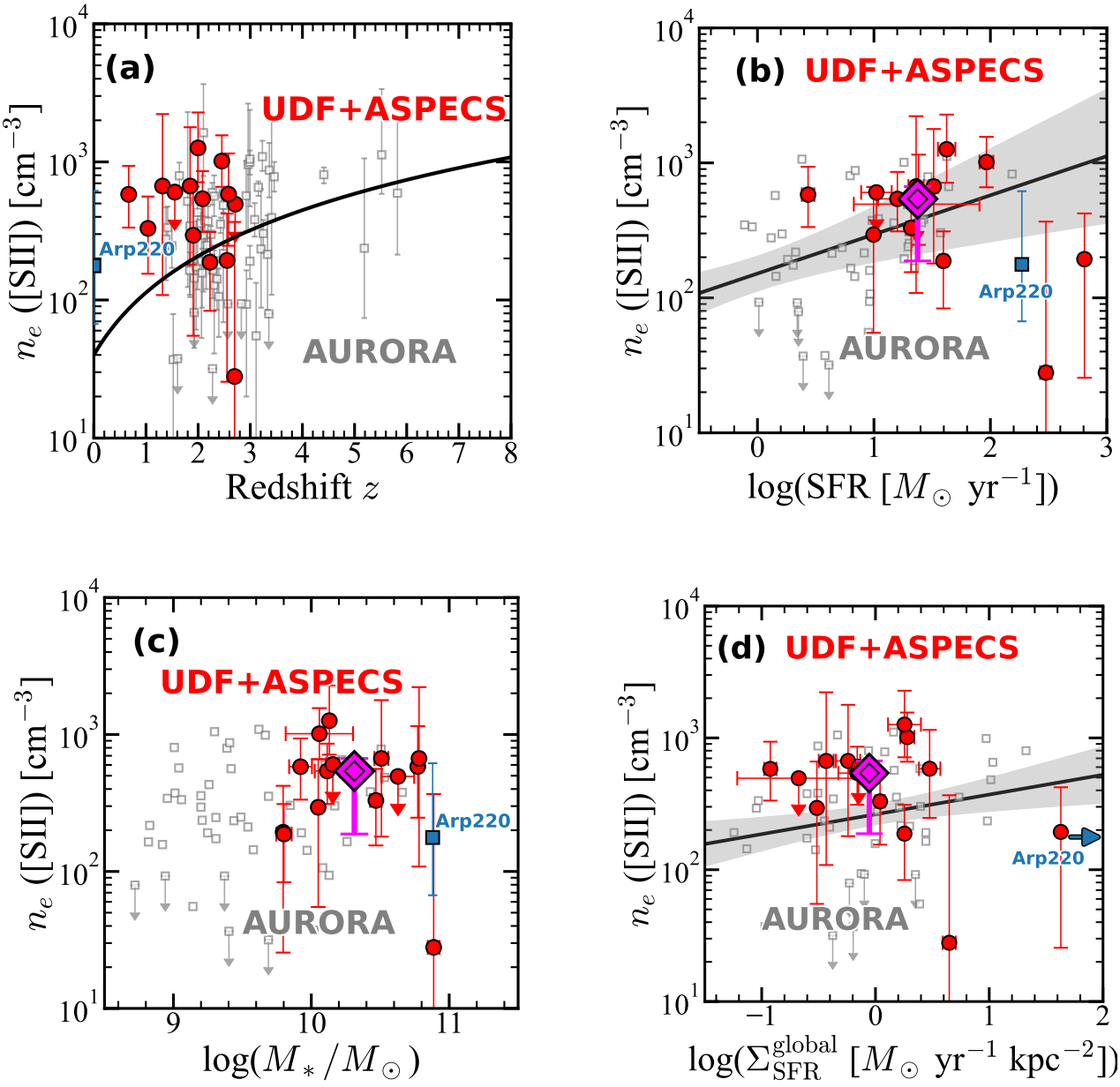

Figure 13. [S II] electron density properties. The red circles show the UDF+ASPECS sample. We compare the electron densities to redshift (a), SFR (b), stellar mass (c), and surface SFR density (d). The magenta double diamonds with errorbars show the median and the 16th–84th percentiles of the UDF+ASPECS sources. For comparison, the AURORA sample at $z = 1.4$–5.8 is plotted as the gray squares (M. W. Topping et al. 2025). The redshift evolution curve (black curve; panel (a)) is quoted from M. W. Topping et al. (2025). The black lines and gray shades in the panels (b) and (d) show the correlations reported in M. W. Topping et al. (2025). For reference, Arp 220, the nearest ULIRG, is shown as blue squares (M. Perna et al. 2020; V. U et al. 2012; M. Pereira-Santaella et al. 2021). Arp 220 has a surface SFR of $\Sigma_{\rm SFR} = 2500\ M_\odot\ {\rm yr}^{-1}$ (M. Pereira-Santaella et al. 2021).

where $D_{\rm L}$ is the luminosity distance, $S_{\nu,\rm obs}$ is the observed flux, $\kappa_{\rm d}(\nu_{\rm rest})$ is the rest-frame dust mass absorption coefficient, and $B_\nu(T_{\rm dust})$ is the Planck function at a rest-frame frequency $\nu_{\rm rest}$ and dust temperature $T_{\rm dust}$. In this equation, $B_\nu(T_{\rm CMB}(z))$ is used to correct for the cosmic microwave background (CMB) effects (e.g., K. Ota et al. 2014). We adopt the emissivity index of $\beta_{\rm IR} = 1.5$, and assume $\kappa_{\rm d}(\nu_{\rm rest}) = 0.77(850\ \mu{\rm m}/\lambda_{\rm rest})^{\beta_{\rm IR}}\ {\rm cm^2\ g^{-1}}$ (L. Dunne et al. 2000), where $\lambda_{\rm rest}$ is the rest-frame wavelength in units of μm. We use $T_{\rm dust} = 40\,{\rm K}$, which is typical for high-redshift galaxies (e.g., M. Aravena et al. 2020; R. Bouwens et al. 2020). In this calculation, we use the 1.3-mm fluxes reported in J. S. Dunlop et al. (2017). The dust masses of the ASPECS sources are derived by M. Aravena et al. (2020) [12], and we utilize them in the following analysis.

Figure 14 shows the dust-to-stellar mass ratio (DTS) and SFR relation. The DTS of UDF+ASPECS sample ranges from log(DTS) ~ -3 to -2. These values are comparable to the local ULIRGs (blue squares) and the ALESS sample (magenta open triangles), indicating that the UDF+ASPECS sources have dust contents similar to those of local ULIRGs and ALESS SMGs. Their high DTS compared to the local galaxies (log(DTS) ~ -3; black open circles) might be due to their higher SFRs.

The left panel of Figure 15 shows the relation between dust-to-gas mass ratio (DTG) and metallicity. We compile gas masses for galaxies with CO emission-line detections from the literature (see Table 1). The UDF+ASPECS sources (red circles) show comparable or smaller DTG compared to the local relation (black dashed and dotted lines; A. Rémy-Ruyer et al. 2014; F. Galliano et al. 2021) and the damped Lyα (DLA) sample (blue square; C. Péroux & J. C. Howk 2020). Compared to the REBELS sample at $z \sim 6$–7, the UDF+ASPECS sources have higher metallicities but similar DTG. The right panel of Figure 15 presents the DTS and metallicity relation (see also, e.g., F. Calura et al. 2017). The UDF+ASPECS sources have higher DTS than local galaxies (Dustpedia; P. De Vis et al. 2019) while being comparable to the DTS of REBELS.

5. DISCUSSION

5.1. *Comparisons with Other Galaxies*

Comparisons with other galaxy populations are useful for characterizing the faint SMGs at high redshift.

[12] M. Aravena et al. (2020) provide SED-based molecular gas masses ($M_{\rm mol,SED}$) by assuming $M_{\rm mol,SED} = 200\,M_{\rm dust}$. We convert them to dust masses via $M_{\rm dust} = M_{\rm mol,SED}/200$ and adopt those values.

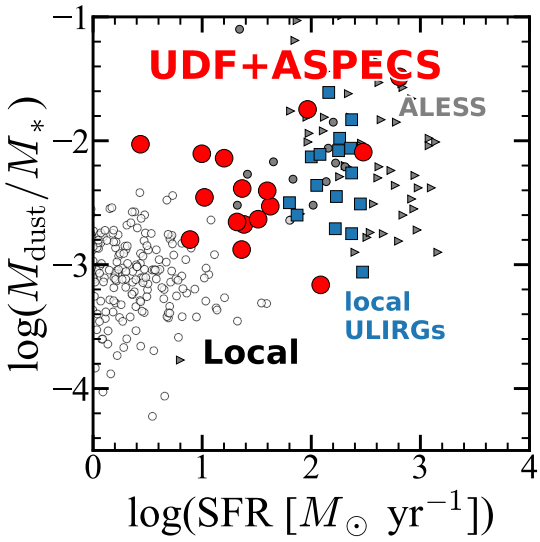

Figure 14. Relation between dust-to-stellar mass ratio (DTS) and SFR. The red circles show the UDF+ASPECS sample. The local galaxies (Dustpedia, black open circle; R. Pavesi et al. 2019), local ULIRGs (blue circles; E. da Cunha et al. 2010), ALESS at $z = 1$–6 (open magenta triangle; E. da Cunha et al. 2015), REBELS at $z = 6$–7 (gray circles; H. Algera et al. 2025; L. E. Rowland et al. 2025) are also shown.

In this section, we compare the UDF+ASPECS sample with other galaxies, including ULIRGs and other SMGs (e.g., ALESS). The UDF+ASPECS sources largely follow the star formation main sequence (Figure 4) and the mass-metallicity relation (Figure 12) at similar redshifts ($z \sim 2$–3). In these aspects, the UDF+ASPECS sources are representative of massive star-forming galaxies at $z \sim 2$. Regarding metallicity, some sources reach nearly solar metallicity, and these values are comparable to those of local ULIRGs (Figure 12; e.g., N. Chartab et al. 2022). This comparison indicates that the metallicity and ISM conditions of the UDF+ASPECS sources are also similar to those of the local ULIRGs and massive star-forming galaxies at high redshift ($z \sim 2$). By contrast, ALESS sources are typically brighter in the dust continuum than the UDF+ASPECS sources, and tend to have higher inferred dust masses and SFRs. These extremely dusty sources can provide deeper insight into the nature of dusty galaxies at high redshift, and JWST follow-up observations will also be important.

5.2. *Critical Metallicity*

With JWST/NIRSpec spectroscopy, we can now directly measure gas-phase metallicities for the faint UDF+ASPECS sample (Section 4.4), enabling a direct comparison between dust mass and chemical enrichment in this population. Figure 16 shows the relation be-

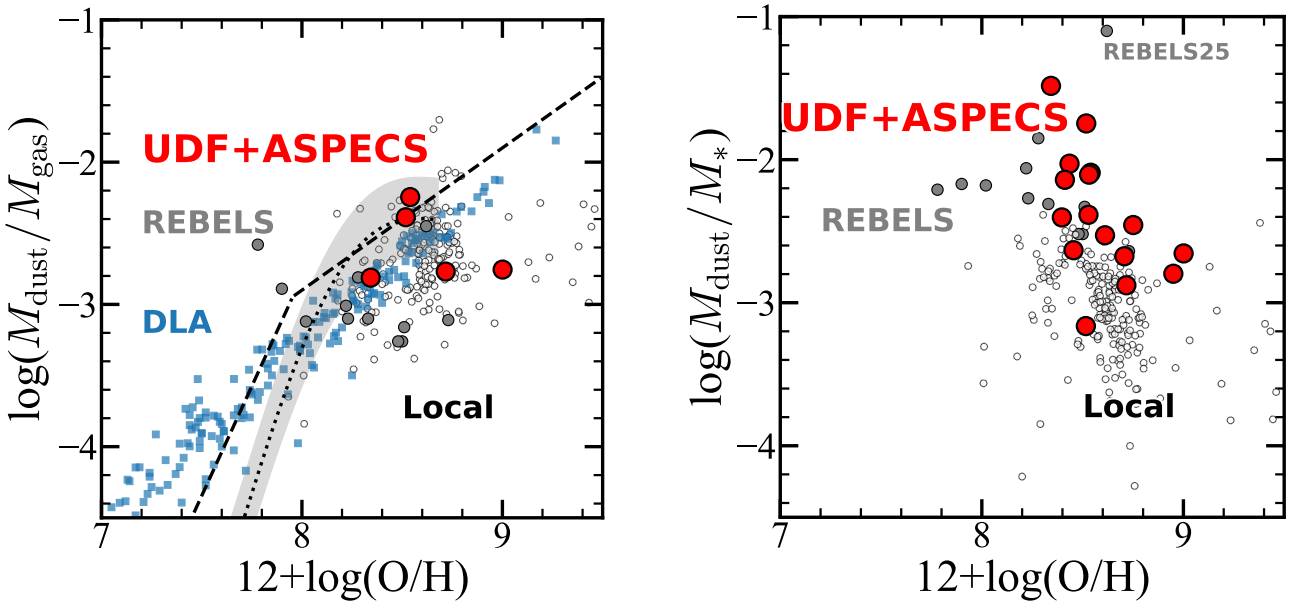

Figure 15. Relation between DTG (DTS) and metallicity is shown in left (right). The red circles show the UDF+ASPECS sample. For the DTG, we only plot the sources with molecular gas mass estimated from the CO lines (M. Aravena et al. 2020). The gray circles, white circles, and blue squares show the REBELS at $z = 6$–7 (L. E. Rowland et al. 2025; H. Algera et al. 2025), local galaxies (Dustpedia; P. De Vis et al. 2019; V. Casasola et al. 2020), and DLA (C. Péroux & J. C. Howk 2020), respectively. The black dashed and dotted lines show local relations (A. Rémy-Ruyer et al. 2014; F. Galliano et al. 2021).

tween dust mass and gas-phase metallicity (see also T. Kiyota et al. 2025). The UDF+ASPECS sources have metallicities above the model-predicted critical metallicity ($Z_{\rm crit} \sim 0.1$–$0.2\,Z_\odot$; e.g., R. S. Asano et al. 2013; A. K. Inoue 2011; S. Zhukovska 2014; D. Burgarella et al. 2025). Above $Z_{\rm crit}$, growth of ISM grain by accretion becomes efficient and can dominate the dust mass build-up. The fact that our SMGs lie above $Z_{\rm crit}$ therefore supports a scenario in which their dust masses are at least partly sustained by ISM grain growth, which naturally explains the dusty nature of the SMGs.

We also find that the UDF+ASPECS sample largely follows the typical DTG-metallicity relation (Figure 15), with DTG values consistent with those of other galaxies at fixed metallicity. This result suggests their dust content is broadly consistent with their chemical enrichment. Consequently, the large dust masses of the UDF+ASPECS sample likely also reflect large gas reservoirs (see also H. Algera et al. 2025 for the REBELS sample), together with above the critical metallicities.

5.3. *Interpretations*

Here, we discuss possible physical interpretations of faint SMGs. Figure 17 summarizes the results of our analysis and previous studies, then presents a possible interpretation as a schematic illustration. As discussed in Section 5.1, the UDF+ASPECS sources largely follow the star-forming main sequence (Figure 4) and mass-metallicity relation (Figure 12). In addition, their electron densities are comparable to those of other star-forming galaxies with similar stellar mass and SFR (Figure 13). These results suggest that the global ISM conditions are not exceptionally extreme, and the UDF+ASPECS sources represent typical massive star-forming galaxies with AGN fraction of $\sim$ 70% (Section 4.2 and Figure 10).

We caution, however, that the [S II] electron density results do not rule out compact starbursts. The [S II] diagnostic saturates above its critical density ($n_{\rm crit} \sim 10^{3.5}\,{\rm cm}^{-3}$) and is therefore insensitive to much higher densities. If nuclear star formation exists, it could still contribute to the observed submillimeter continuum. One example is Arp 220 (e.g., H. Arp 1966), the nearest ULIRG, which shows the [S II] electron density of n_e([S II]) = 170 cm^{-3} (Figure 13; e.g., M. Perna et al. 2020). Its electron density from [Fe II] 1.644 μm, 1.677 μm is n_e([Fe II]) $\sim$ 5000 cm^{-3} especially around the nuclear outflow region (L. Ulivi et al. 2025). The critical density of [Fe II] is higher ($n_{\rm crit} \sim 10^4\,{\rm cm}^{-3}$) than that of [S II], and [Fe II] can trace the higher density gas (L. Ulivi et al. 2025).

The FIR sizes of ALMA-selected galaxies are often more compact than their rest-frame UV/optical sizes,

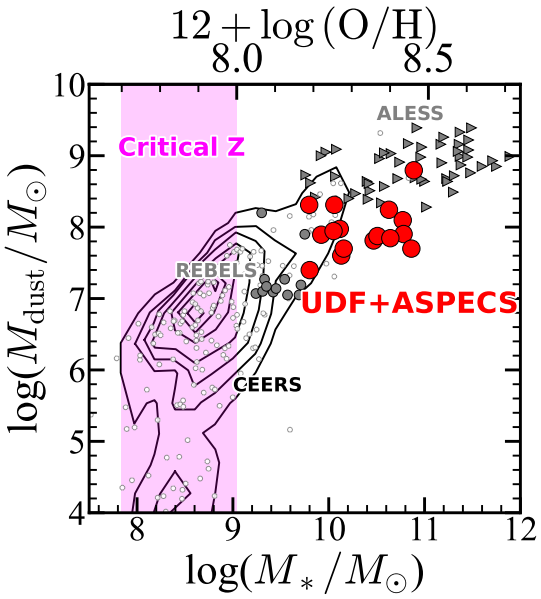

Figure 16. Relation between dust mass and stellar mass. The red circles show the UDF+ASPECS sample. The gray triangles and circles show the ALESS and REBELS samples, respectively. The background white circles show the JWST Cosmic Evolution Early Release Science (CEERS) survey galaxies at $4 < z < 11$ reported in D. Burgarella et al. (2025), and the black contours show their distribution. The dust mass of the CEERS galaxies is estimated from rest-frame UV-NIR SED fitting. The magenta shaded band indicates the model-predicted critical metallicity (0.1–$0.2Z_{\odot}$; R. S. Asano et al. 2013; D. Burgarella et al. 2025). The ticks at the top represent metallicity, converted from stellar mass, using the mass–metallicity relation at $z = 4$–10 as presented in K. Nakajima et al. (2023).

supporting compact star formation (e.g., S. Fujimoto et al. 2017; W. Rujopakarn et al. 2016; D. Elbaz et al. 2018; M. Kaasinen et al. 2020; C. Gómez-Guijarro et al. 2022b). For the ALMA UDF sources, we compile literature measurements from D. Elbaz et al. (2018) and find the median effective radius of R_e(FIR) = 1.77 kpc and R_e(UV) = 3.15 kpc (HST/WFC3 H band). Consistent with this picture, L. A. Boogaard et al. (2024) find that the sizes of the ASPECS sources measured in JWST/MIRI F560W, which corresponds to their NIR wavelength, are smaller than those in HST F160W (R_e(F560W)/R_e(F160W) ~ 0.7). These multi-wavelength size offsets are naturally explained by centrally concentrated, dust-obscured star formation (and/or stronger dust attenuation toward the inner regions), which likely governs the observed FIR emission (see Figure 17).

For individual sources in the UDF+ASPECS sample, UDF2 and UDF7 are analyzed in W. Rujopakarn et al. (2019) based on the high-resolution (30 mas, 200 pc) ALMA Band 7 data. They report compact dust emission on $\sim$ 1–3 kpc scale and surrounding UV-emitting clumps with no dust detections. These results further support a picture of compact FIR dust emission (see also W. Rujopakarn et al. 2023).

Regarding AGN activity, previous studies (P. F. Hopkins et al. 2008; S. Toft et al. 2014) suggest that dusty galaxies can be progenitors of AGNs and QSOs based on their number density and gas depletion timescales. The high fraction of AGN (Figure 10), even in the faint SMGs, is consistent with these scenarios and provides direct evidence of the co-evolution of the stellar mass growth and supermassive black hole growth (see also S. Fujimoto et al. 2022).

We note that AGN heating may also contribute to dust emission, and could potentially affect even the FIR continuum (e.g., K. Nandra & K. Iwasawa 2007; M. Symeonidis et al. 2016; M. Symeonidis 2017; J. McKinney et al. 2021; T. Tsukui et al. 2023). If AGN UV radiation escapes to the ISM scales, it can contribute to dust heating and may also be observed as the cold dust emission ($T_{\rm dust} \sim 40$ K). The dust continuum emission peaks of the faint SMGs are sometimes located near the central regions of the sources (Figures 6–8), raising the possibility that some of the dust emission is associated with central AGN activity. However, other discussions also argue for a smaller FIR component from AGNs than that from star-formation based on the bright QSO studies (e.g., J. D. Silverman et al. 2025). The current ALMA dust continuum data of the UDF and ASPECS have limited spatial resolution ($\sim 1''$). It remains challenging to determine the relative contributions of AGN activity and compact, nuclear star formation to the FIR dust emission. Future high-resolution ALMA dust continuum observations can be useful for determining the origins of the FIR emission.

To discuss the physical properties of ALMA-detected galaxies, it is useful to examine the ALMA detection fraction as a function of stellar mass. Figure 18 shows the fraction of galaxies at $z = 1.5$–3.5 detected in the UDF and/or ASPECS programs, which have spectroscopic redshifts from JADES or SMILES. We define ALMA-detected sources as those reported in Table 2 of J. S. Dunlop et al. (2017) or Table 1 of M. Aravena et al. (2020). We construct the parent sample from the JADES and SMILES spectroscopic catalogs by selecting sources within the ASPECS footprint where the ALMA primary-beam response (PB) satisfies PB > 0.2 (e.g., J. González-López et al. 2020). We then restrict the sample to $z = 1.5$–3.5 using the spectroscopic redshifts provided in the JADES or SMILES catalog. The stellar masses of all sources in this analysis are esti-

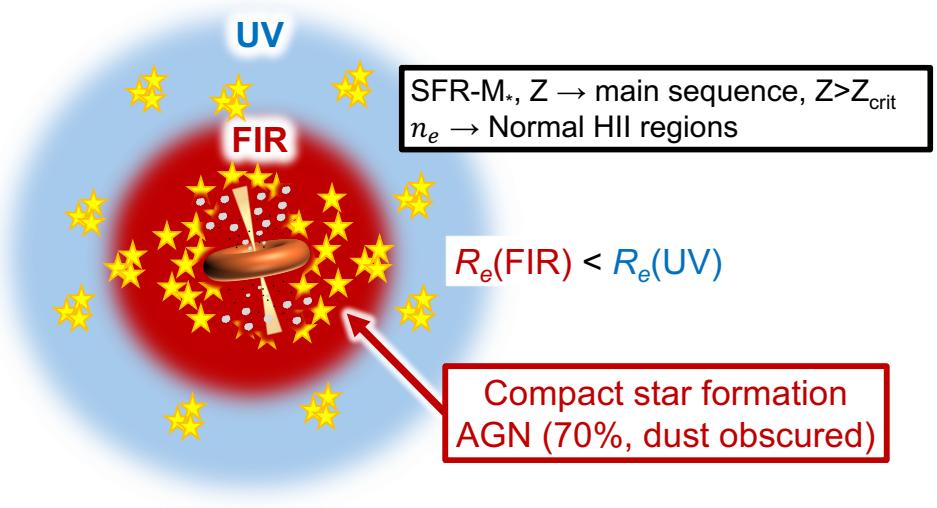

Figure 17. Schematic illustration of a possible physical picture for ALMA-detected galaxies, motivated by the UDF+ASPECS sample and literature. Previous work has shown that FIR size is more compact than UV size (R_e(FIR) < R_e(UV)) and that faint SMGs typically lie on the star-forming main sequence. In this study, the ISM properties are broadly consistent with those of other star-forming galaxies (metallicity and [S II] electron density). We also identify that ∼ 70% sources host AGNs, and most of them are obscured (type-2). In this scenario, compact central star formation and AGN activity produce a compact FIR component, yielding R_e(FIR) < R_e(UV) (FIR: red; UV/optical: blue). Because the [S II] doublet has a relatively low critical density ($n_e \sim 10^3$ cm^{-3}), [S II] primarily traces the bulk star-forming ISM rather than the highest-density gas near the nucleus. The metallicity exceeds the critical value ($Z_{\rm crit}$), placing these galaxies in a regime where efficient dust growth can proceed.

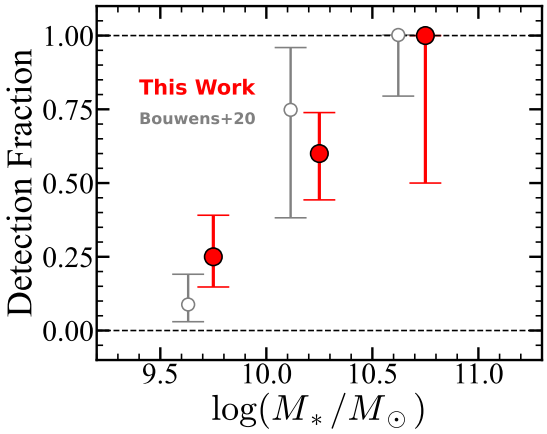

Figure 18. Relation between the fraction of galaxies at z = 1.5–3.5 that are detected in the UDF or ASPECS programs and stellar mass. The errorbars show the binomial proportion confidence intervals. We only use galaxies that have $z_{\rm spec}$ from JADES and SMILES. The stellar mass bins are $\log(M_*/M_\odot)$ = 9.5–10.0, 10.0–10.5, and 10.5–11.0. The open circles show the fraction calculated in R. Bouwens et al. (2020) based on HST photo-z galaxies and the ASPECS-detected sources where the ASPECS 1σ continuum sensitivity is the highest (< 20 μJy beam^{-1}).

mated with the empirical calibration between $M_{\rm F444W}$ and $\log(M_*/M_\odot)$ as described in Section 4.2.

Figure 18 indicates that the detection fraction is ∼ 60% and ∼ 100% at $\log(M_*/M_\odot)$ = 10.0–10.5 and $\log(M_*/M_\odot) > 10.5$, respectively. The detection fraction decreases toward lower stellar masses, likely reflecting the limited depth of the current ALMA data for low-mass systems. R. Bouwens et al. (2020) report a consistent trend using HST photometry as a parent sample (open circles in Figure 18). These results indicate that ALMA sources provide an efficient census of the most massive star-forming galaxies at $z \sim$ 2–3. Taken together, we explore the representatives of the massive star-forming galaxies and their rest-frame optical spectroscopic properties using dust continuum emission as a tracer.

6. SUMMARY AND CONCLUSIONS

We present JWST/NIRSpec rest-frame optical spectroscopic ceusus of 16 ALMA 1-mm flux-limited sources in the HUDF. Our parent sample is taken from the ALMA UDF and ASPECS deep surveys ($S_{1\,\rm mm} \gtrsim$ 0.1 mJy). From these sources, we select those with medium-resolution NIRSpec spectra available from the public JWST surveys, JADES, and SMILES. The resulting sample covers $z_{\rm spec}$ = 1–4 and $\log(L_{\rm IR}/L_\odot)$ = 11–13. Our findings and discussions are summarized as follows:

1. We explore the rest-frame optical emission lines of Hβ, [O III]$\lambda\lambda$4959, 5007, Hα, [N II]$\lambda\lambda$6548, 6584, [S II]$\lambda\lambda$6717, 6731. We obtain a nebular attenuation of $E(B-V) \sim$ 0.3–1.8 for 12 sources. For the

remaining four sources, the Hβ line is not detected, which implies $E(B-V) > 1.0$.

2. Based on the Chandra X-ray data and the BPT diagram, nearly 70% (11/16) of the UDF+ASPECS sources are classified as AGNs. We find that only one source shows prominent broad Balmer lines (Hα and Hβ, FWHM$_{\rm H\alpha} \sim 6500$ km s^{-1}) with narrow [O III] lines, indicating type-1 AGN. These results suggest that the faint SMGs preferentially host obscured AGNs.

3. The [S II] electron densities are $n_e \sim 10^2$–10^3 cm^{-3}, comparable to those of other star-forming galaxies with similar stellar mass, and SFR. The metallicities estimated from the N2 index are moderately high ($12 + \log({\rm O/H}) = 8.3$–$9.0$; i.e., $Z = 0.4$–$2Z_\odot$), suggesting that these faint SMGs are above the critical metallicity for efficient dust growth.

4. The UDF+ASPECS sample is mainly on the SFR–M_*, mass–metallicity, and dust mass–other properties (e.g., stellar mass, gas mass) relation, indicating that these sources show the representatives of massive star-forming galaxies at similar redshifts. Combining the previous reports on the galaxy morphologies (R_e(FIR) $<$ R_e(UV)), these sources show compact star-formation, obscured (type-2) AGNs, and a bulk of the ISM conditions comparable to those of the other star-forming galaxies.

ACKNOWLEDGMENTS

The authors thank Masatoshi Imanishi, Nozomu Kawakatsu, Yurina Nakazato, and Yoshiki Toba for the valuable comments and discussions. T.K. thanks Ryosuke Uematsu for technical support with the SED analysis.

This work is based in part on observations made with the NASA/ESA/CSA James Webb Space Telescope. The data were obtained from the Mikulski Archive for Space Telescopes at the Space Telescope Science Institute, which is operated by the Association of Universities for Research in Astronomy, Inc., under NASA contract NAS 5-03127 for JWST. These observations are associated with programs GTO-1180, GTO-1181, GTO-1210, GTO-1286, GTO-1287, GO-3215 (JADES), GO-1963 (JEMS), GTO-1207 (SMILES). The authors acknowledge the JADES (PIs: Daniel J. Eisenstein, Nora Luetzgendorf, and Kate Isaak), JEMS (PI: Christina C. Williams), and SMILES (PI: George Rieke) for developing their observing program with a zero-exclusive-access period. All the JWST data used in this paper can be found in MAST: 10.17909/8tdj-8n28, 10.17909/fsc4-dt61, and 10.17909/et3f-zd57.

Data analysis was in part carried out on the Multi-wavelength Data Analysis System operated by the Astronomy Data Center (ADC), National Astronomical Observatory of Japan.

This publication is based upon work supported by the World Premier International Research Center Initiative (WPI Initiative), MEXT, Japan, KAKENHI (21H04489, 22H04939, 23K20035, 24H00004, 25H00674) through the Japan Society for the Promotion of Science, and JST FOREST Program (JP-MJFR202Z). This work was supported by the joint research program of the Institute for Cosmic Ray Research (ICRR), University of Tokyo. S.F. acknowledges support from the Dunlap Institute, funded through an endowment established by the David Dunlap family and the University of Toronto. Y.U. acknowledges the support from the Kyoto University Foundation. M.N. is supported by JST, the establishment of university fellowships towards the creation of science technology innovation, Grant Number JPMJFS2136. The English writing in this paper has been improved with the help of ChatGPT and Grammarly, while the software does not generate sentences from scratch.

Facilities: JWST (NIRSpec, NIRCam, MIRI)

Software: Astropy (Astropy Collaboration et al. 2013, 2018, 2022), CIGALE (D. Burgarella et al. 2005; S. Noll et al. 2009; M. Boquien et al. 2019; G. Yang et al. 2020, 2022), Matplotlib (J. D. Hunter 2007), NumPy (C. R. Harris et al. 2020), pandas (W. McKinney 2010) PyNeb (V. Luridiana et al. 2015), SciPy (P. Virtanen et al. 2020),

APPENDIX

Table 4. CIGALE Modules and Parameters

Parameter	Symbol	Value
Delayed SFH and recent burst (`shfdelayedbq`; L. Ciesla et al. 2017)		
e-folding time of the main stellar population	$\log(\tau_{\rm main})$ (Myr)	[2.0, 4.1] (step 0.3)
Age of the main stellar population	$\log(\rm age_{main})$ (Myr)	[2.0, 4.1] (step 0.3)
Age of the burst and quench episode	$\rm age_{bq}$ (Myr)	10, 100
Ratio of the SFR after/before $\rm age_{bq}$	$R_{\rm SFR}$	1, 10, 100, 1000
SSP (`bc03`; G. Bruzual & S. Charlot 2003)		
Initial mass function	···	G. Chabrier (2003)
Metallicity	Z	0.008, 0.02
Attenuation law (`dustatt_modified_starburst`; D. Calzetti et al. 2000; C. Leitherer et al. 2002)		
Color excess of the nebular lines light	$E(B-V)_{\rm lines}$	0.1, [0.3, 2.4] (step 0.3)
Factor for the stellar continuum attenuation	$E(B-V)_{\rm factor}$	0.44
Power law slope for the attenuation curve	δ	[−0.8, 0.4] (step 0.4)
Dust emission (`themis`; A. P. Jones et al. 2017)		
Mass fraction of hydrocarbon solids	$q_{\rm hac}$	0.02, 0.06, 0.10, 0.14, 0.20, 0.28, 0.36
Minimum radiation field	$U_{\rm min}$	0.6, 1.5, 4.0, 10, 25, 50
Power law slope of $dU/dM \propto U^{\alpha}$	α	2.0
Fraction illuminated from $U_{\rm min}$ to $U_{\rm max}$	γ	0.02
AGN (`skirtor2016`; M. Stalevski et al. 2012, 2016)		
Average edge-on optical depth at 9.7 μm	$\tau_{9.7}$	5, 9
Inclination angle	i (°)	30, 70
AGN fraction	$f_{\rm AGN}$	0.0, 0.05, [0.1, 0.9] (step 0.2)
Temperature of polar dust	T (K)	150

Note—Other parameters are the same as the CIGALE default values.

A. CIGALE PARAMETERS

In Table 4, we summarize the parameters used for the SED fitting with CIGALE (Section 3.2).

REFERENCES

Ahumada, R., Allende Prieto, C., Almeida, A., et al. 2020, ApJS, 249, 3, doi: 10.3847/1538-4365/ab929e

Akaike, H. 1974, IEEE Transactions on Automatic Control, 19, 716, doi: 10.1109/TAC.1974.1100705

Alberts, S., Lyu, J., Shivaei, I., et al. 2024, ApJ, 976, 224, doi: 10.3847/1538-4357/ad7396

Algera, H., Rowland, L., Stefanon, M., et al. 2025, arXiv e-prints, arXiv:2501.10508, doi: 10.48550/arXiv.2501.10508

Aravena, M., Decarli, R., Gónzalez-López, J., et al. 2019, ApJ, 882, 136, doi: 10.3847/1538-4357/ab30df

Aravena, M., Boogaard, L., Gónzalez-López, J., et al. 2020, ApJ, 901, 79, doi: 10.3847/1538-4357/ab99a2

Arp, H. 1966, ApJS, 14, 1, doi: 10.1086/190147

Arribas, S., Perna, M., Rodríguez Del Pino, B., et al. 2024, A&A, 688, A146, doi: 10.1051/0004-6361/202348824

Asano, R. S., Takeuchi, T. T., Hirashita, H., & Inoue, A. K. 2013, Earth, Planets and Space, 65, 213, doi: 10.5047/eps.2012.04.014

Asplund, M., Grevesse, N., Sauval, A. J., & Scott, P. 2009, ARA&A, 47, 481, doi: 10.1146/annurev.astro.46.060407.145222

Astropy Collaboration, Robitaille, T. P., Tollerud, E. J., et al. 2013, A&A, 558, A33, doi: 10.1051/0004-6361/201322068

Astropy Collaboration, Price-Whelan, A. M., Sipőcz, B. M., et al. 2018, AJ, 156, 123, doi: 10.3847/1538-3881/aabc4f

Astropy Collaboration, Price-Whelan, A. M., Lim, P. L., et al. 2022, ApJ, 935, 167, doi: 10.3847/1538-4357/ac7c74

Baldwin, J. A., Phillips, M. M., & Terlevich, R. 1981, PASP, 93, 5, doi: 10.1086/130766
Beckwith, S. V. W., Stiavelli, M., Koekemoer, A. M., et al. 2006, AJ, 132, 1729, doi: 10.1086/507302
Blain, A. W., & Longair, M. S. 1993, MNRAS, 264, 509, doi: 10.1093/mnras/264.2.509
Blain, A. W., Smail, I., Ivison, R. J., Kneib, J. P., & Frayer, D. T. 2002, PhR, 369, 111, doi: 10.1016/S0370-1573(02)00134-5
Bodansky, S., Whitaker, K. E., Abdullah, A., et al. 2025, arXiv e-prints, arXiv:2507.19472, doi: 10.48550/arXiv.2507.19472
Boogaard, L. A., Decarli, R., González-López, J., et al. 2019, ApJ, 882, 140, doi: 10.3847/1538-4357/ab3102
Boogaard, L. A., Gillman, S., Melinder, J., et al. 2024, ApJ, 969, 27, doi: 10.3847/1538-4357/ad43e5
Boquien, M., Burgarella, D., Roehlly, Y., et al. 2019, A&A, 622, A103, doi: 10.1051/0004-6361/201834156
Bouchet, P., García-Marín, M., Lagage, P. O., et al. 2015, PASP, 127, 612, doi: 10.1086/682254
Bouwens, R., González-López, J., Aravena, M., et al. 2020, ApJ, 902, 112, doi: 10.3847/1538-4357/abb830
Bouwens, R. J., Smit, R., Schouws, S., et al. 2022, ApJ, 931, 160, doi: 10.3847/1538-4357/ac5a4a
Bradford, C. M. M., Kogut, A. J., Fixsen, D., et al. 2025, Journal of Astronomical Telescopes, Instruments, and Systems, 11, 031627, doi: 10.1117/1.JATIS.11.3.031627
Bruzual, G., & Charlot, S. 2003, MNRAS, 344, 1000, doi: 10.1046/j.1365-8711.2003.06897.x
Burgarella, D., Buat, V., & Iglesias-Páramo, J. 2005, MNRAS, 360, 1413, doi: 10.1111/j.1365-2966.2005.09131.x
Burgarella, D., Buat, V., Theulé, P., et al. 2025, A&A, 699, A336, doi: 10.1051/0004-6361/202554231
Calura, F., Pozzi, F., Cresci, G., et al. 2017, MNRAS, 465, 54, doi: 10.1093/mnras/stw2749
Calzetti, D., Armus, L., Bohlin, R. C., et al. 2000, ApJ, 533, 682, doi: 10.1086/308692
Capak, P. L., Carilli, C., Jones, G., et al. 2015, Nature, 522, 455, doi: 10.1038/nature14500
Carlstrom, J. E., Ade, P. A. R., Aird, K. A., et al. 2011, PASP, 123, 568, doi: 10.1086/659879
Carvalho, S. P., Dors, O. L., Cardaci, M. V., et al. 2020, MNRAS, 492, 5675, doi: 10.1093/mnras/staa193
Casasola, V., Bianchi, S., De Vis, P., et al. 2020, A&A, 633, A100, doi: 10.1051/0004-6361/201936665
Casey, C. M., Narayanan, D., & Cooray, A. 2014, PhR, 541, 45, doi: 10.1016/j.physrep.2014.02.009
Casey, C. M., Cooray, A., Killi, M., et al. 2017, ApJ, 840, 101, doi: 10.3847/1538-4357/aa6cb1
Casey, C. M., Kartaltepe, J. S., Drakos, N. E., et al. 2023, ApJ, 954, 31, doi: 10.3847/1538-4357/acc2bc
Cathey, J., Gonzalez, A. H., Lower, S., et al. 2024, ApJ, 967, 11, doi: 10.3847/1538-4357/ad33c9
Chabrier, G. 2003, PASP, 115, 763, doi: 10.1086/376392
Chartab, N., Cooray, A., Ma, J., et al. 2022, Nature Astronomy, 6, 844, doi: 10.1038/s41550-022-01679-y
Cheng, C., Huang, J.-S., Smail, I., et al. 2023, ApJL, 942, L19, doi: 10.3847/2041-8213/aca9d0
Ciesla, L., Elbaz, D., & Fensch, J. 2017, A&A, 608, A41, doi: 10.1051/0004-6361/201731036
Cooper, O. R., Brammer, G., Heintz, K. E., et al. 2025, ApJ, 982, 125, doi: 10.3847/1538-4357/adb8e1
Curti, M., Mannucci, F., Cresci, G., & Maiolino, R. 2020, MNRAS, 491, 944, doi: 10.1093/mnras/stz2910
Curtis-Lake, E., Cameron, A. J., Bunker, A. J., et al. 2025, arXiv e-prints, arXiv:2510.01033, doi: 10.48550/arXiv.2510.01033
da Cunha, E., Charmandaris, V., Díaz-Santos, T., et al. 2010, A&A, 523, A78, doi: 10.1051/0004-6361/201014498
da Cunha, E., Walter, F., Smail, I. R., et al. 2015, ApJ, 806, 110, doi: 10.1088/0004-637X/806/1/110
De Vis, P., Jones, A., Viaene, S., et al. 2019, A&A, 623, A5, doi: 10.1051/0004-6361/201834444
Decarli, R., Walter, F., Gónzalez-López, J., et al. 2019, ApJ, 882, 138, doi: 10.3847/1538-4357/ab30fe
D'Eugenio, F., Cameron, A. J., Scholtz, J., et al. 2025, ApJS, 277, 4, doi: 10.3847/1538-4365/ada148
Dudzevičiūtė, U., Smail, I., Swinbank, A. M., et al. 2020, MNRAS, 494, 3828, doi: 10.1093/mnras/staa769
Dunlop, J. S., McLure, R. J., Biggs, A. D., et al. 2017, MNRAS, 466, 861, doi: 10.1093/mnras/stw3088
Dunne, L., Eales, S., Edmunds, M., et al. 2000, MNRAS, 315, 115, doi: 10.1046/j.1365-8711.2000.03386.x
Duras, F., Bongiorno, A., Ricci, F., et al. 2020, A&A, 636, A73, doi: 10.1051/0004-6361/201936817
Eisenstein, D. J., Willott, C., Alberts, S., et al. 2023, arXiv e-prints, arXiv:2306.02465, doi: 10.48550/arXiv.2306.02465
Eisenstein, D. J., Johnson, B. D., Robertson, B., et al. 2025, ApJS, 281, 50, doi: 10.3847/1538-4365/ae1137
Elbaz, D., Leiton, R., Nagar, N., et al. 2018, A&A, 616, A110, doi: 10.1051/0004-6361/201732370
Franco, M., Elbaz, D., Béthermin, M., et al. 2018, A&A, 620, A152, doi: 10.1051/0004-6361/201832928
Fujimoto, S., Ouchi, M., Ono, Y., et al. 2016, ApJS, 222, 1, doi: 10.3847/0067-0049/222/1/1
Fujimoto, S., Ouchi, M., Shibuya, T., & Nagai, H. 2017, ApJ, 850, 83, doi: 10.3847/1538-4357/aa93e6

Fujimoto, S., Brammer, G. B., Watson, D., et al. 2022, Nature, 604, 261, doi: 10.1038/s41586-022-04454-1
Fujimoto, S., Kohno, K., Ouchi, M., et al. 2024, ApJS, 275, 36, doi: 10.3847/1538-4365/ad5ae2
Fujimoto, S., Bezanson, R., Labbe, I., et al. 2025, ApJS, 278, 45, doi: 10.3847/1538-4365/adc677
Galliano, F., Nersesian, A., Bianchi, S., et al. 2021, A&A, 649, A18, doi: 10.1051/0004-6361/202039701
Gardner, J. P., Mather, J. C., Abbott, R., et al. 2023, PASP, 135, 068001, doi: 10.1088/1538-3873/acd1b5
Genzel, R., Lutz, D., Sturm, E., et al. 1998, ApJ, 498, 579, doi: 10.1086/305576
Giacconi, R., Zirm, A., Wang, J., et al. 2002, ApJS, 139, 369, doi: 10.1086/338927
Giavalisco, M., Ferguson, H. C., Koekemoer, A. M., et al. 2004, ApJL, 600, L93, doi: 10.1086/379232
Gillman, S., Smail, I., Gullberg, B., et al. 2024, A&A, 691, A299, doi: 10.1051/0004-6361/202451006
Glenn, J., Meixner, M., Bradford, C. M., et al. 2025, Journal of Astronomical Telescopes, Instruments, and Systems, 11, 031628, doi: 10.1117/1.JATIS.11.3.031628
Gómez-Guijarro, C., Toft, S., Karim, A., et al. 2018, ApJ, 856, 121, doi: 10.3847/1538-4357/aab206
Gómez-Guijarro, C., Elbaz, D., Xiao, M., et al. 2022a, A&A, 658, A43, doi: 10.1051/0004-6361/202141615
Gómez-Guijarro, C., Elbaz, D., Xiao, M., et al. 2022b, A&A, 658, A43, doi: 10.1051/0004-6361/202141615
González-López, J., Novak, M., Decarli, R., et al. 2020, ApJ, 897, 91, doi: 10.3847/1538-4357/ab765b
Greene, J. E., Labbe, I., Goulding, A. D., et al. 2024, ApJ, 964, 39, doi: 10.3847/1538-4357/ad1e5f
Grogin, N. A., Kocevski, D. D., Faber, S. M., et al. 2011, ApJS, 197, 35, doi: 10.1088/0067-0049/197/2/35
Harris, C. R., Millman, K. J., van der Walt, S. J., et al. 2020, Nature, 585, 357, doi: 10.1038/s41586-020-2649-2
Hatsukade, B., Kohno, K., Yamaguchi, Y., et al. 2018, PASJ, 70, 105, doi: 10.1093/pasj/psy104
Hodge, J. A., & da Cunha, E. 2020, Royal Society Open Science, 7, 200556, doi: 10.1098/rsos.200556
Hodge, J. A., Karim, A., Smail, I., et al. 2013, ApJ, 768, 91, doi: 10.1088/0004-637X/768/1/91
Hodge, J. A., da Cunha, E., Kendrew, S., et al. 2025, ApJ, 978, 165, doi: 10.3847/1538-4357/ad9a52
Holland, W. S., Robson, E. I., Gear, W. K., et al. 1999, MNRAS, 303, 659, doi: 10.1046/j.1365-8711.1999.02111.x
Hopkins, P. F., Hernquist, L., Cox, T. J., & Kereš, D. 2008, ApJS, 175, 356, doi: 10.1086/524362
Hunter, J. D. 2007, Computing in Science & Engineering, 9, 90, doi: 10.1109/MCSE.2007.55
Iani, E., Caputi, K. I., Rinaldi, P., et al. 2024, ApJ, 963, 97, doi: 10.3847/1538-4357/ad15f6
Ikeda, R., Iono, D., Tadaki, K.-i., et al. 2025, arXiv e-prints, arXiv:2510.18006, doi: 10.48550/arXiv.2510.18006
Illingworth, G. D., Magee, D., Oesch, P. A., et al. 2013, ApJS, 209, 6, doi: 10.1088/0067-0049/209/1/6
Inoue, A. K. 2011, MNRAS, 415, 2920, doi: 10.1111/j.1365-2966.2011.18906.x
Jakobsen, P., Ferruit, P., Alves de Oliveira, C., et al. 2022, A&A, 661, A80, doi: 10.1051/0004-6361/202142663
Jones, A. P., Köhler, M., Ysard, N., Bocchio, M., & Verstraete, L. 2017, A&A, 602, A46, doi: 10.1051/0004-6361/201630225
Jones, G. C., Übler, H., Perna, M., et al. 2024, A&A, 682, A122, doi: 10.1051/0004-6361/202347838
Jones, G. C., Bunker, A. J., Telikova, K., et al. 2025, MNRAS, 540, 3311, doi: 10.1093/mnras/staf899
Juodžbalis, I., Maiolino, R., Baker, W. M., et al. 2025, arXiv e-prints, arXiv:2504.03551, doi: 10.48550/arXiv.2504.03551
Kaasinen, M., Walter, F., Novak, M., et al. 2020, ApJ, 899, 37, doi: 10.3847/1538-4357/aba438
Kauffmann, G., Heckman, T. M., Tremonti, C., et al. 2003, MNRAS, 346, 1055, doi: 10.1111/j.1365-2966.2003.07154.x
Kewley, L. J., Dopita, M. A., Leitherer, C., et al. 2013, ApJ, 774, 100, doi: 10.1088/0004-637X/774/2/100
Kewley, L. J., Dopita, M. A., Sutherland, R. S., Heisler, C. A., & Trevena, J. 2001, ApJ, 556, 121, doi: 10.1086/321545
Kiyota, T., Ouchi, M., Xu, Y., et al. 2025, ApJ, 995, 150, doi: 10.3847/1538-4357/ae1cc3
Kokorev, V., Fujimoto, S., Labbe, I., et al. 2023, ApJL, 957, L7, doi: 10.3847/2041-8213/ad037a
Kormendy, J., & Ho, L. C. 2013, ARA&A, 51, 511, doi: 10.1146/annurev-astro-082708-101811
Lehmer, B. D., Brandt, W. N., Alexander, D. M., et al. 2005, ApJS, 161, 21, doi: 10.1086/444590
Leitherer, C., Li, I. H., Calzetti, D., & Heckman, T. M. 2002, ApJS, 140, 303, doi: 10.1086/342486
Liu, F.-Y., Dunlop, J. S., McLure, R. J., et al. 2026, MNRAS, 545, staf1961, doi: 10.1093/mnras/staf1961
Luo, B., Brandt, W. N., Xue, Y. Q., et al. 2017, ApJS, 228, 2, doi: 10.3847/1538-4365/228/1/2
Luridiana, V., Morisset, C., & Shaw, R. A. 2015, A&A, 573, A42, doi: 10.1051/0004-6361/201323152
Lyu, J., Alberts, S., Rieke, G. H., et al. 2024, ApJ, 966, 229, doi: 10.3847/1538-4357/ad3643
Maiolino, R., Scholtz, J., Curtis-Lake, E., et al. 2024, A&A, 691, A145, doi: 10.1051/0004-6361/202347640

Marrone, D. P., Spilker, J. S., Hayward, C. C., et al. 2018, Nature, 553, 51, doi: 10.1038/nature24629
McKinney, J., Hayward, C. C., Rosenthal, L. J., et al. 2021, ApJ, 921, 55, doi: 10.3847/1538-4357/ac185f
McKinney, J., Casey, C. M., Long, A. S., et al. 2025, ApJ, 979, 229, doi: 10.3847/1538-4357/ada357
McKinney, W. 2010, in Proceedings of the 9th Python in Science Conference, ed. S. van der Walt & J. Millman, 56 – 61, doi: 10.25080/Majora-92bf1922-00a
Mizukoshi, S., Minezaki, T., Sameshima, H., et al. 2024, MNRAS, 532, 666, doi: 10.1093/mnras/stae1482
Nakajima, K., Ouchi, M., Isobe, Y., et al. 2023, ApJS, 269, 33, doi: 10.3847/1538-4365/acd556
Nandra, K., & Iwasawa, K. 2007, MNRAS, 382, L1, doi: 10.1111/j.1745-3933.2007.00372.x
Nishigaki, M., Nakajima, K., Ouchi, M., et al. 2025, arXiv e-prints, arXiv:2512.12983, doi: 10.48550/arXiv.2512.12983
Noll, S., Burgarella, D., Giovannoli, E., et al. 2009, A&A, 507, 1793, doi: 10.1051/0004-6361/200912497
Oke, J. B., & Gunn, J. E. 1983, ApJ, 266, 713, doi: 10.1086/160817
Osterbrock, D. E., & Ferland, G. J. 2006, Astrophysics of gaseous nebulae and active galactic nuclei (University Science Books)
Ota, K., Walter, F., Ohta, K., et al. 2014, ApJ, 792, 34, doi: 10.1088/0004-637X/792/1/34
Parlanti, E., Carniani, S., Übler, H., et al. 2024, A&A, 684, A24, doi: 10.1051/0004-6361/202347914
Parlanti, E., Carniani, S., Venturi, G., et al. 2025, A&A, 695, A6, doi: 10.1051/0004-6361/202451692
Pavesi, R., Riechers, D. A., Faisst, A. L., Stacey, G. J., & Capak, P. L. 2019, ApJ, 882, 168, doi: 10.3847/1538-4357/ab3a46
Peng, C. Y., Ho, L. C., Impey, C. D., & Rix, H.-W. 2002, AJ, 124, 266, doi: 10.1086/340952
Pereira-Santaella, M., Colina, L., García-Burillo, S., et al. 2021, A&A, 651, A42, doi: 10.1051/0004-6361/202140955
Perna, M., Arribas, S., Catalán-Torrecilla, C., et al. 2020, A&A, 643, A139, doi: 10.1051/0004-6361/202038328
Péroux, C., & Howk, J. C. 2020, ARA&A, 58, 363, doi: 10.1146/annurev-astro-021820-120014
Pilbratt, G. L., Riedinger, J. R., Passvogel, T., et al. 2010, A&A, 518, L1, doi: 10.1051/0004-6361/201014759
Planck Collaboration, Aghanim, N., Akrami, Y., et al. 2020, A&A, 641, A6, doi: 10.1051/0004-6361/201833910
Poglitsch, A., Waelkens, C., Geis, N., et al. 2010, A&A, 518, L2, doi: 10.1051/0004-6361/201014535
Reines, A. E., & Volonteri, M. 2015, ApJ, 813, 82, doi: 10.1088/0004-637X/813/2/82
Rémy-Ruyer, A., Madden, S. C., Galliano, F., et al. 2014, A&A, 563, A31, doi: 10.1051/0004-6361/201322803
Ren, J., Liu, F. S., Li, N., et al. 2025, ApJ, 982, 200, doi: 10.3847/1538-4357/adb961
Riechers, D. A., Bradford, C. M., Clements, D. L., et al. 2013, Nature, 496, 329, doi: 10.1038/nature12050
Rieke, G. H., Alberts, S., Shivaei, I., et al. 2024, ApJ, 975, 83, doi: 10.3847/1538-4357/ad6cd2
Rieke, G. H., Wright, G. S., Böker, T., et al. 2015, PASP, 127, 584, doi: 10.1086/682252
Rieke, G. H., Sun, Y., Lyu, J., et al. 2025, ApJ, 994, 35, doi: 10.3847/1538-4357/adff79
Rieke, M. J., Robertson, B., Tacchella, S., et al. 2023a, ApJS, 269, 16, doi: 10.3847/1538-4365/acf44d
Rieke, M. J., Kelly, D. M., Misselt, K., et al. 2023b, PASP, 135, 028001, doi: 10.1088/1538-3873/acac53
Rigby, J. R., Diamond-Stanic, A. M., & Aniano, G. 2009, ApJ, 700, 1878, doi: 10.1088/0004-637X/700/2/1878
Robertson, B., Johnson, B. D., Tacchella, S., et al. 2024, ApJ, 970, 31, doi: 10.3847/1538-4357/ad463d
Rowland, L. E., Stefanon, M., Bouwens, R., et al. 2025, arXiv e-prints, arXiv:2501.10559, doi: 10.48550/arXiv.2501.10559
Rujopakarn, W., Dunlop, J. S., Rieke, G. H., et al. 2016, ApJ, 833, 12, doi: 10.3847/0004-637X/833/1/12
Rujopakarn, W., Daddi, E., Rieke, G. H., et al. 2019, ApJ, 882, 107, doi: 10.3847/1538-4357/ab3791
Rujopakarn, W., Williams, C. C., Daddi, E., et al. 2023, ApJL, 948, L8, doi: 10.3847/2041-8213/accc82
Rynkun, P., Gaigalas, G., & Jönsson, P. 2019, A&A, 623, A155, doi: 10.1051/0004-6361/201834931
Sanders, R. L., Shapley, A. E., Kriek, M., et al. 2016, ApJ, 816, 23, doi: 10.3847/0004-637X/816/1/23
Sanders, R. L., Shapley, A. E., Jones, T., et al. 2021, ApJ, 914, 19, doi: 10.3847/1538-4357/abf4c1
Santini, P., Fontana, A., Castellano, M., et al. 2017, ApJ, 847, 76, doi: 10.3847/1538-4357/aa8874
Schlafly, E. F., & Finkbeiner, D. P. 2011, ApJ, 737, 103, doi: 10.1088/0004-637X/737/2/103
Scholtz, J., Carniani, S., Parlanti, E., et al. 2025, arXiv e-prints, arXiv:2510.01034, doi: 10.48550/arXiv.2510.01034
Shapley, A. E., Cullen, F., Dunlop, J. S., et al. 2020, ApJL, 903, L16, doi: 10.3847/2041-8213/abc006
Shapley, A. E., Sanders, R. L., Topping, M. W., et al. 2025, ApJ, 980, 242, doi: 10.3847/1538-4357/adad68
Shivaei, I., Alberts, S., Florian, M., et al. 2024, A&A, 690, A89, doi: 10.1051/0004-6361/202449579

Shuntov, M., Akins, H. B., Paquereau, L., et al. 2025, arXiv e-prints, arXiv:2506.03243, doi: 10.48550/arXiv.2506.03243

Silverman, J. D., Daddi, E., Tan, Q.-H., et al. 2025, arXiv e-prints, arXiv:2509.20548, doi: 10.48550/arXiv.2509.20548

Smail, I., Ivison, R. J., & Blain, A. W. 1997, ApJL, 490, L5, doi: 10.1086/311017

Spilker, J. S., Phadke, K. A., Aravena, M., et al. 2023, Nature, 618, 708, doi: 10.1038/s41586-023-05998-6

Stalevski, M., Fritz, J., Baes, M., Nakos, T., & Popović, L. Č. 2012, MNRAS, 420, 2756, doi: 10.1111/j.1365-2966.2011.19775.x

Stalevski, M., Ricci, C., Ueda, Y., et al. 2016, MNRAS, 458, 2288, doi: 10.1093/mnras/stw444

Storey, P. J., & Zeippen, C. J. 2000, MNRAS, 312, 813, doi: 10.1046/j.1365-8711.2000.03184.x

Straatman, C. M. S., Spitler, L. R., Quadri, R. F., et al. 2016, ApJ, 830, 51, doi: 10.3847/0004-637X/830/1/51

Sun, F., Yang, J., Wang, F., et al. 2025, arXiv e-prints, arXiv:2506.06418, doi: 10.48550/arXiv.2506.06418

Swinbank, A. M., Smail, I., Chapman, S. C., et al. 2004, ApJ, 617, 64, doi: 10.1086/425171

Symeonidis, M. 2017, MNRAS, 465, 1401, doi: 10.1093/mnras/stw2784

Symeonidis, M., Giblin, B. M., Page, M. J., et al. 2016, MNRAS, 459, 257, doi: 10.1093/mnras/stw667

Tayal, S. S., & Zatsarinny, O. 2010, ApJS, 188, 32, doi: 10.1088/0067-0049/188/1/32

Tielens, A. G. G. M. 2008, ARA&A, 46, 289, doi: 10.1146/annurev.astro.46.060407.145211

Toft, S., Smolčić, V., Magnelli, B., et al. 2014, ApJ, 782, 68, doi: 10.1088/0004-637X/782/2/68

Topping, M. W., Sanders, R. L., Shapley, A. E., et al. 2025, MNRAS, 541, 1707, doi: 10.1093/mnras/staf903

Tsukui, T., Wisnioski, E., Krumholz, M. R., & Battisti, A. 2023, MNRAS, 523, 4654, doi: 10.1093/mnras/stad1464

U, V., Sanders, D. B., Mazzarella, J. M., et al. 2012, ApJS, 203, 9, doi: 10.1088/0067-0049/203/1/9

Übler, H., D'Eugenio, F., Perna, M., et al. 2024, MNRAS, 533, 4287, doi: 10.1093/mnras/stae1993

Ueda, Y., Hashimoto, Y., Ichikawa, K., et al. 2015, ApJ, 815, 1, doi: 10.1088/0004-637X/815/1/1

Ueda, Y., Hatsukade, B., Kohno, K., et al. 2018, ApJ, 853, 24, doi: 10.3847/1538-4357/aa9f10

Ulivi, L., Perna, M., Lamperti, I., et al. 2025, A&A, 693, A36, doi: 10.1051/0004-6361/202451442

Umehata, H., Tamura, Y., Kohno, K., et al. 2015, ApJL, 815, L8, doi: 10.1088/2041-8205/815/1/L8

van der Wel, A., Bell, E. F., Häussler, B., et al. 2012, ApJS, 203, 24, doi: 10.1088/0067-0049/203/2/24

Virtanen, P., Gommers, R., Oliphant, T. E., et al. 2020, Nature Methods, 17, 261, doi: 10.1038/s41592-019-0686-2

Walter, F., Decarli, R., Aravena, M., et al. 2016, ApJ, 833, 67, doi: 10.3847/1538-4357/833/1/67

Wang, S. X., Brandt, W. N., Luo, B., et al. 2013, ApJ, 778, 179, doi: 10.1088/0004-637X/778/2/179

Weibel, A., Oesch, P. A., Barrufet, L., et al. 2024, MNRAS, 533, 1808, doi: 10.1093/mnras/stae1891

Weisskopf, M. C., Brinkman, B., Canizares, C., et al. 2002, PASP, 114, 1, doi: 10.1086/338108

Williams, C. C., Tacchella, S., Maseda, M. V., et al. 2023, ApJS, 268, 64, doi: 10.3847/1538-4365/acf130

Wootten, A., & Thompson, A. R. 2009, IEEE Proceedings, 97, 1463, doi: 10.1109/JPROC.2009.2020572

Wright, G. S., Rieke, G. H., Glasse, A., et al. 2023, PASP, 135, 048003, doi: 10.1088/1538-3873/acbe66

Xu, Y., Ouchi, M., Nakajima, K., et al. 2025, ApJ, 984, 182, doi: 10.3847/1538-4357/adc733

Xue, Y. Q., Luo, B., Brandt, W. N., et al. 2011, ApJS, 195, 10, doi: 10.1088/0067-0049/195/1/10

Yang, G., Boquien, M., Buat, V., et al. 2020, MNRAS, 491, 740, doi: 10.1093/mnras/stz3001

Yang, G., Boquien, M., Brandt, W. N., et al. 2022, ApJ, 927, 192, doi: 10.3847/1538-4357/ac4971

York, D. G., Adelman, J., Anderson, Jr., J. E., et al. 2000, AJ, 120, 1579, doi: 10.1086/301513

Zhu, Y., Bonaventura, N., Sun, Y., et al. 2025, arXiv e-prints, arXiv:2508.12599, doi: 10.48550/arXiv.2508.12599

Zhukovska, S. 2014, A&A, 562, A76, doi: 10.1051/0004-6361/201322989